MASARYKOVA UNIVERZITA
PŘÍRODOVĚDECKÁ FAKULTA
ÚSTAV TEORETICKÉ FYZIKY A ASTROFYZIKY

Bakalářská práce

BRNO 2024 MARTIN MONDEK

MASARYKOVA
UNIVERZITA
PŘÍRODOVĚDECKÁ FAKULTA
ÚSTAV TEORETICKÉ FYZIKY A ASTROFYZIKY

Vlastnosti kvaziperiodických erupcí v galaktických jádrech

Bakalářská práce

Martin Mondek

Vedoucí práce: RNDr. Michal Zajaček, PhD. **Brno 2024**

Bibliografický záznam

Autor:	Martin Mondek Přírodovědecká fakulta, Masarykova univerzita Ústav teoretické fyziky a astrofyziky
Název práce:	Vlastnosti kvaziperiodických erupcí v galaktických jádrech
Studijní program:	Fyzika
Studijní obor:	Astrofyzika
Vedoucí práce:	RNDr. Michal Zajaček, PhD.
Akademický rok:	2023/2024
Počet stran:	$60 + \mathrm{xvii}$
Klíčová slova:	Klíčová slova: Aktivní galaktická jádra, Slapové trhání hvězdy, RTG záření, Periodogram, EMRI, Akreční disk, Proměnnost na časových škálách

Bibliographic Entry

Author:	Martin Mondek Faculty of Science, Masaryk University Department of Theoretical Physics and Astrophysics
Title of Thesis:	Properties of quasi-periodic eruptions in active galactic nuclei
Degree Programme:	Physics
Field of Study:	Astrophysics
Supervisor:	RNDr. Michal Zajaček, PhD.
Academic Year:	2023/2024
Number of Pages:	$60 + \text{xvii}$
Keywords:	Keywords:Active galactic nuclei, TDEs, X-ray radiation, Periodogram, EMRI, Accretion disk, Timescale variabilities

Abstrakt

V této práci se budeme věnovat analýze zcela nového jevu, který se vyskytuje v aktivních galaktických jádrech. Tyto události dostaly název kvazi-periodické erupce

(QPEs). Předpona ”kvazi” byla vybrána proto, aby popsala časové úseky mezi jednotlivými erupcemi, které nejsou konstantní. Porovnáme zde jejich základní fyzikální vlastnosti a budeme se snažit přijít na to, proč některé spolu souvisí. Dále analyzujeme periodu jednotlivých zdrojů (jejichž světelné křivky máme k dispozici) pomocí 3 různých algoritmů. Podíváme se také na konkrétní fyzikální model systému, který se snaží replikovat světelné křivky pro dané zdroje. Modifikací tohoto modelu se také pokusíme vytvořit umělé světelné křivky, a nakonec učiníme předpověď pro chování konkrétních QPE zdrojů v budoucím čase.

Abstract

In this work, we focus on analyzing new phenomena occurring in active galactic nuclei (AGNs). These are called quasi-periodic eruptions (QPEs). The prefix ”quasi” has been chosen to describe the time intervals between following eruptions that are not constant. We focus on visualizing the main physical properties and then attempt to come up with reasons why some of them are connected. In the following part, 3 types of periodograms for each source will be presented. We also adopt a physical model of a system that tries to duplicate measured light curves and create artificial light curves as well. The last small section is dedicated to some basic forecasts about the long-term evolution of the selected sources.

MUNI
SCI

MASARYKOVA UNIVERZITA
PŘÍRODOVĚDECKÁ FAKULTA
KOTLÁŘSKÁ 2, 611 37 BRNO
IČ: 00216224
DIČ: CZ00216224

ZADÁNÍ BAKALÁŘSKÉ PRÁCE

Akademický rok: 2023/2024

Ústav:	Ústav teoretické fyziky a astrofyziky
Student:	Martin Mondek
Program:	Fyzika
Specializace:	Astrofyzika

Ředitel *ústavu* PřF MU Vám ve smyslu Studijního a zkušebního řádu MU určuje bakalářskou práci s názvem:

Název práce:	Vlastnosti kvaziperiodických erupcí v galaktických jádrech
Název práce anglicky:	Properties of quasiperiodic eruptions in galactic nuclei
Jazyk závěrečné práce:	angličtina

Oficiální zadání:

The growth and the evolution of supermassive black holes (hereafter SMBHs) is one of the fundamental problems of modern astrophysics. SMBHs accrete from the surrounding accretion disks and the accretion rate is typically stochastic, characterized as a red-noise process, i.e. the amplitude of variability rises towards longer timescales as a power-law function. However, some galactic nuclei exhibit peaks in the luminosity that deviate from the red-noise flickering. In recent years, X-ray satellites have detected a few sources, where such large ourbursts repeat in a quasi-periodic way every few hours or days. They were called Quisiperiodic Eruptions (QPEs). These outbursts exceed the quiescent level by one to two orders of magnitude in flux density and their spectral energy distributions are consistent with being thermal with the characteristic temperature of about million Kelvins. In this bachelor thesis, the student will consider X-ray light curves of the known QPE sources. The student will characterize the power spectral densities of the light curves, in particular, they will compare the power spectral density slopes and the periodogram peaks among individual sources. Next, they will study correlations between the basic quantities, e.g. the mean period vs. flare duration or other characteristics determined from X-ray spectra or host galaxies (flare temperature, SMBH mass etc). Finally, the student will evaluate the shape of the flares (their degree of symmetry/asymmetry) and they will discuss the result in the astrophysical context. For example, they may consider a model of the formation of a small accretion disk that is quickly consumed or shocks between the streams of gas moving relativistically around the SMBH. Depending on the student's interests, they may consider just one source in detail or consider all known QPE sources. In addition, a physical model may be constructed to interpret/fit the observed flares.

Literatura:

KARAS, Vladimír, Jiří SVOBODA a Michal ZAJAČEK. *Selected Chapters on Active Galactic Nuclei as Relativistic Systems*. Opava: Institute of Physics, Silesian University in Opava, 2021. 154 s. Lecture notes. ISBN 978-80-7510-475-5.

Vedoucí práce:	RNDr. Michal Zajaček, PhD.
Konzultant:	Mgr. Ing. arch. Petr Kurfürst, Ph.D.
Datum zadání práce:	29. 6. 2023
V Brně dne:	20. 2. 2024

Martin Mondek, 12. 11. 2023
RNDr. Michal Zajaček, PhD., 13. 11. 2023
RNDr. Luboš Poláček, 5. 12. 2023

Poděkování

Na tomto místě bych rád poděkoval svému vedoucímu, doktoru Michalu Zajačkovi, za spolupráci a ochotu, a hlavně motivaci. Dále patří mé díky doktoru Kurfürstovi za pomoc s náležitostmi bakalářské práce, a Elišce Pavlíkové za úpravu anglického jazyka. Nakonec bych rád poděkoval za data světelných křivek, které poskytl: G. Miniutti, PhD., R. Arcodia, PhD., a D. R. Pasham PhD.

Prohlášení

Prohlašuji, že jsem svoji bakalářskou práci vypracoval samostatně pod vedením vedoucího práce s využitím informačních zdrojů, které jsou v práci citovány.

Brno 12. května 2024 .....

Martin Mondek

Contents

Introduction

Active galactic nuclei (AGN) are thr cores of $\sim 10\%$ of all galaxies. Most of the time, a galaxy contains a massive black hole in the core with a mass of 10^4–$10^{10}\,M_\odot$. For example, our Galaxy contains a dormant supermassive black hole that is not part of an active nucleus (it does not accrete mass converting it into energy). We could say that a galaxy's core is active with material like stars, gas, or dust around to feed on it. That creates a big energy output with a wide range of electromagnetic radiation spanning always over the IR, optical, and UV parts, but in rare cases (like quasars) it covers all parts of the spectrum. A typical AGN is a very complicated system containing a massive black hole, accretion disk, broad-line region, narrow-line region, dusty torus, and with certain conditions for accretion, the black hole sheds material in the form of collimated jets (relativistically moving material).

The interest in this area of astrophysics has grown a lot over the last few decades ($\geq$ 1000 articles/year). As we can observe all parts of the electromagnetic radiation coming from AGNs we can gather reliable estimates about their length scales, masses of central black holes, physical processes - thermal processes like accretion, non–thermal processes, reprocessing of the radiation, and much more. For example, with only a few variable parameters such as a black hole mass and spin, inclination of the accretion disk with respect to the black hole spin, and the accretion rate, the AGN provides perfect laboratory conditions for models of accretion - spherical, Bondi-Hoyle accretion, efficiency of accretion, and so on.

These nuclei can be also variable on short or long timescales depending on the mechanism in play. It depends on where in the electromagnetic spectrum we look for these variabilities. For example, the short variability can be caused by an external companion that crashes with the accretion disk. The companion could be a star, for example, a main-sequence star, or a more compact star, like a neutron star or a black hole. The companion does not need to interact with anything since its obstruction of the view of AGN can cause variability as well. Accretion disk instabilities - precession of the disk so fast that it divides the disk into multiple thick rings that start to precess with their own angular frequency; this is another example of short variability timescales. Gravitational lensing of two black holes could be an example of a short but also a long-term variability.

In this work, the focus will be on very short timescales on the order of tens of minutes to days. This relatively new phenomenon was observed for the first time 5 years ago in galaxy GSN 069. From then until now, 6 other sources were observed. Every few hours or so a quiescent level of an accretion disk is interrupted by eruptions lasting for 2–3 hours. The problem is in the fact that the eruptions are not periodic, i.e. they repeat with a variable period, hence the prefix quasi- for the name Quasi-Periodic Eruptions, which is the main

and only focus of this bachelor thesis. There are more quasi- properties, such as the peak luminosities of the eruptions that change as well but stay around a value of $\sim 10^{42}\,\mathrm{erg.s}^{-1}$. We will briefly talk about the properties of individual sources.

This thesis is organised as follows: In the chapter 1: Active Galactic Nuclei we talk about the most basic facts concerning active galactic nuclei. Our aim is to explain this topic graphically and not quantitatively, with equations. Chapter 2: Introduction to QPEs is only about QPEs. What are they, what are their properties, when they were observed, and how their light curves look like, are questions we answer. Chapter 3: Model of Perturber Crashing with an Accretion Disk is an oversimplified recapitulation of the article (Franchini, Alessia et al., 2023) that tries to explain the nature of 4 QPE sources through their own model based on extreme mass ratio inspiral (EMRI) system. We then simplify the model and attempt to recreate the light curves on our own. In Chapter 4: Statistics of QPEs we firstly make statistics with correlations of different QPE properties, we create periodograms on sources we have data on, and try to predict the long-term evolution of the eRO-QPE1 system. In the final section, we adopt a Toy model based on the article from Chapter 3 and create artificial light curves through that model. In 5.3 we explain how periodograms, that we used in this thesis, theoretically work.

This new AGN phenomenon is exciting to study because we can learn a thing or two about accretion disks and how they behave around extremely massive objects. It could clarify some types of accretion modes or force us to invent new ones. It is also another nice framework of general relativity to be tested experimentally. If QPEs are the case of EMRI systems we would have great candidates for gravitational wave observations with the upcoming LISA observatory that would be sensitive enough to measure these ripples of spacetime.

Active Galactic Nuclei

1.1 Main Characteristics

Active galactic nuclei (AGNs) are cores of galaxies that are unique with their high luminosities that often span over all parts of the electromagnetic spectrum. Most of the cores have a luminosity peak in UV (Big Blue Bump) and emit light strongly in X-ray. That kind of emission depends on whether the nucleus emits relativistically moving material in collimated jets out into galactic space. The central part of the nucleus itself is a black hole with mass in the range of $10^{6-10}\,\mathrm{M}_\odot$ that emits radiation through the accretion of the surrounding material in the shape of a circular accretion disk.

The spectral energy distribution (SED) of normal galaxy nuclei can be obtained as the superposition of thermal spectra produced by the stars with different surface temperatures. Effective temperatures of the stars lie somewhere between 3000 K and 40 000 K which points to SED spanned only over infrared, optical, and ultraviolet parts. Therefore, different physical processes are present in AGNs than are missing in most of the galaxies. A typical representation of AGN SED is in the Fig. 1.1. In a narrow energy span the SED can be described by a power-law function

$$L_\nu \propto \nu^{-\alpha}. \tag{1.1}$$

The idea of a galactic nucleus is sketched in the Fig. 1.2.

1.2 Brief History of a Galactic Nucleus

The most central object serving as a central engine of the entire galaxy is a supermassive black hole (SMBH). Its presence was proposed to explain large jets (as long as megaparsecs) and emitted energies in over $10^{40}\,\mathrm{erg.s}^{-1}$, as well as the variabilities on short timescales (even days). There are two most prominent scenarios for the creation of MBHs, as of today. They are created from the surrounding material of stars and gas; both involve a gaseous molecular disk at the start:

1. Massive hydrogen-helium stars started to form after the recombination epoch a few hundred million years after the Big Bang. They produced seed black holes of 10–100 M_{BH} that accreted mass from the surrounding environment. The gaseous molecular disks cooled mostly through H_2 cooling and through fragmentation, stars were formed afterwards.

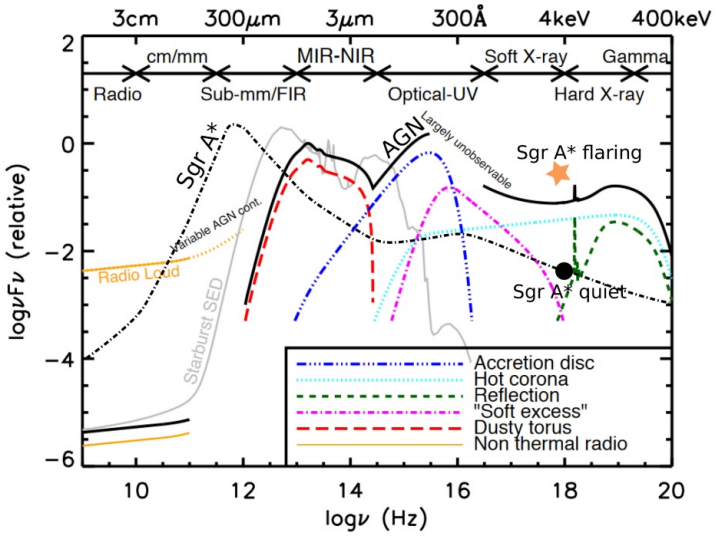

Figure 1.1: Illustration of an AGN spectral energy distribution. The resulting SED is marked with a solid black line, while its components are coloured. Credit: (Karas et al., 2021).

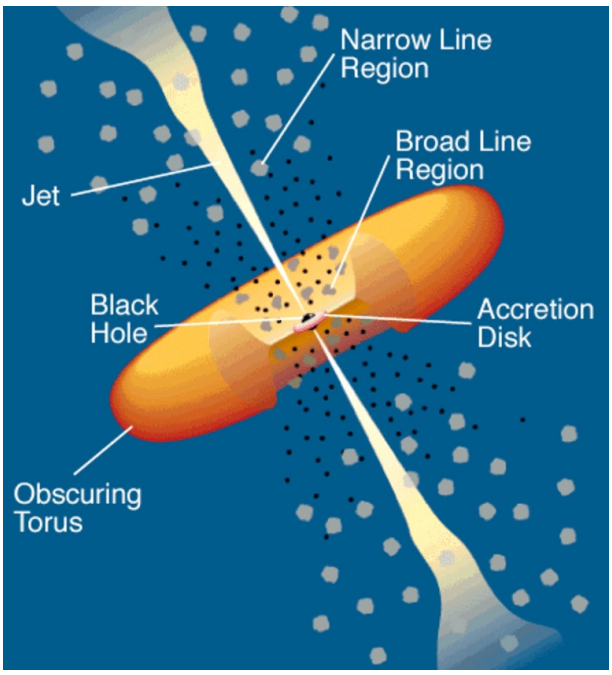

Figure 1.2: Simplified diagram of AGN. Credit: (Urry and Padovani, 1995)

2. In the second case that was proposed more recently, the disk contains mainly atomic hydrogen that cools much more slowly (with a mechanism of external irradiation that makes the forming of H_2 uneasy.) The disk becomes gravitationally unstable, and all the matter is led into the centre directly.

The only problem with scenario 1. is that the mass of the black hole does not reach sufficient values we see today. However, there are many solutions for this including the direct collapse of a gaseous disk. Both cases are illustrated in the Fig. 1.3.

In most of the galaxies, the SMBHs are surrounded by clusters of gas and stars – Nuclear Star Clusters (NSCs). These are very compact and massive clusters of stars comparable with their properties to globular clusters. Their luminosities can overshine the whole nuclei regions, especially in the case of non-active galactic nuclei. NSCs exist in a vast range of different host environments which makes a long way of intensive research about their origin that is far from finished. Although NSCs seem like globular clusters just inside galaxies their brightness and compactness stand out as demonstrated in the Fig. 1.4.

On the right, it can be seen that NSCs are very often the brightest clusters in their host galaxies. The masses of nuclear star clusters correlate with galaxy masses, but higher-mass galaxies have a lower fraction of their mass in their NSCs (Neumayer et al., 2020).

Now we have a black hole as a central object with a star cluster surrounding it scaled on a diameter of tens of parsecs. Another essential part of an active nucleus is an accretion disk (with enough matter). Its creation can have multiple origins, but all share the same concept: whenever the matter SMBH accretes has enough angular momentum so that it cannot fall straightly inward it forms an accretion disk (with enough matter, off course). This structure is a material in motion around the black hole. Gravitational and frictional forces raise the temperature of the material and that creates electromagnetic radiation that can glow in infrared up to the X-ray part of the spectrum. Instabilities in the disk cause the infall of the material towards the SMBH. The infall of the material (accretion) can explain large luminosities in some AGNs because for compact objects such as black holes the conversion of matter into energy is very effective (tens of percents). In the case of spherical stationary accretion onto SMBH it is possible to calculate the maximum accretion luminosity where spherical accretion stops working and a more sophisticated model of accretion needs to be implemented.

With an assumption that a black hole is surrounded by ionized hydrogen gas and that radiation pressure force mostly pushes on electrons we can come out with an expression for the maximum luminosity called the *Eddington luminosity*:

$$L_{\mathrm{Edd}} = \frac{4\pi G M_\bullet m_\mathrm{p} c}{\sigma_\mathrm{T}} = 1.3 \cdot 10^{46} \left(\frac{\mathrm{M}_\bullet}{10^8 \mathrm{M}_\odot} \right) \mathrm{erg.s}^{-1}, \tag{1.2}$$

where G is a gravitational constant, $M_\bullet$ is the mass of the black hole, m_p the mass of the proton, c the speed of light, and σ_T Thomson's cross-section of an electron. The ratio of the observed luminosity to the Eddington luminosity is called the Eddington ratio, $\lambda_{\mathrm{Edd}} \equiv L_{\mathrm{bol}}/L_{\mathrm{Edd}}$. Most of the AGN luminosities are with Eddington ratio below 1 and contain a geometrically thick accretion disk. In the case of super-Eddington luminosities, $\lambda_{\mathrm{Edd}} \geq 1$ slim disks come to the action.

Based on the virial theorem, the accretion luminosity can be expressed as

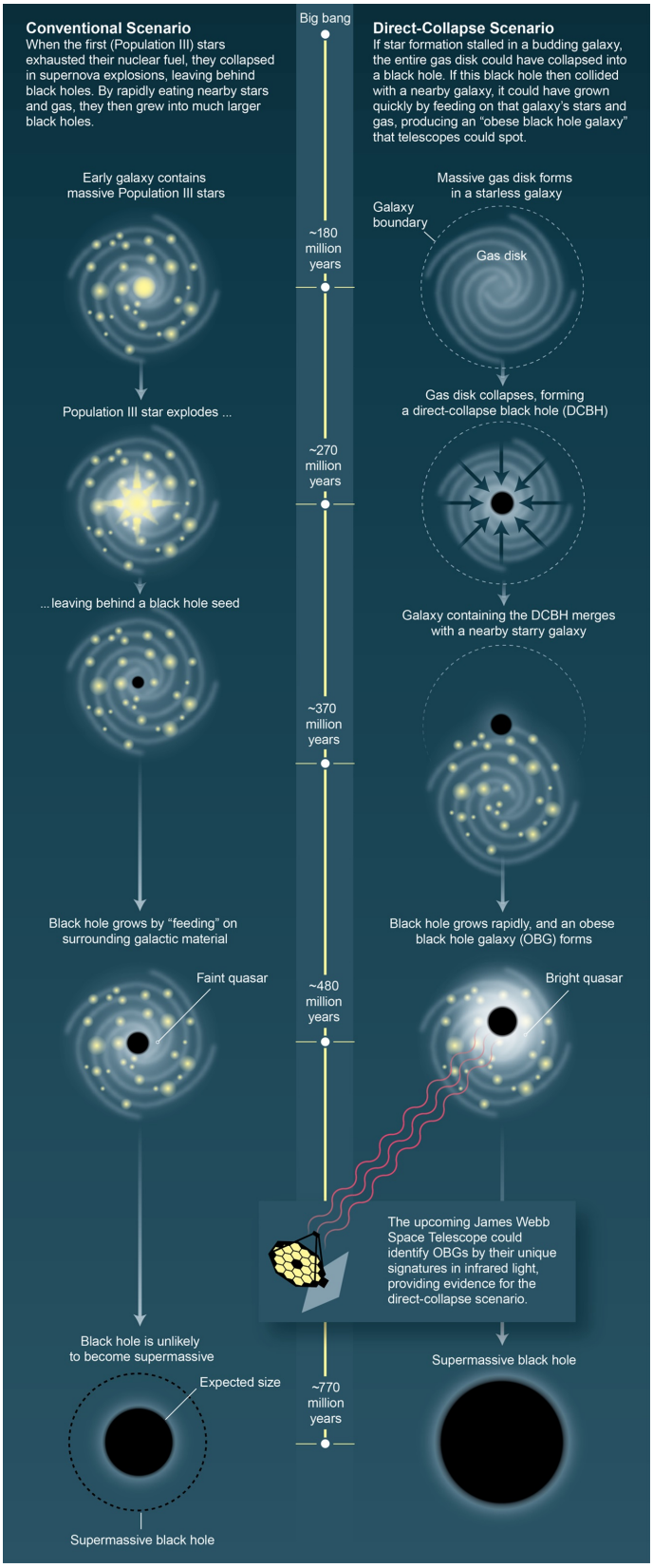

Figure 1.3: Two ways to make a massive black hole. (Natarajan, 2018)

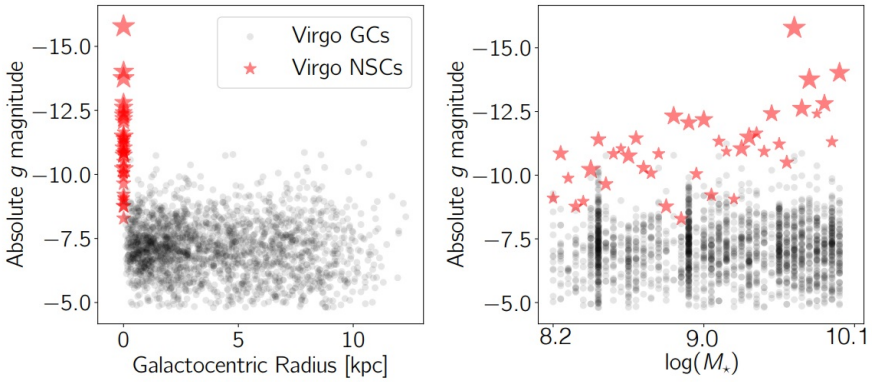

Figure 1.4: Comparison of NSCs and globular clusters in the Virgo cluster. The left panel shows the radial distribution of the clusters vs. their g-band luminosity. The right panel shows the distribution of globular clusters and NSCs's absolute magnitudes separately for each galaxy, and ordered by host stellar mass. (Neumayer et al., 2020)

$$L_{\rm acc} = \frac{GM_\bullet \dot{M}_{\rm acc}}{2R_0} \tag{1.3}$$

where R_0 is the initial radius from which the matter falls onto the black hole and $\dot{M}$ the accretion rate. Here, hot gas circles around the SMBH until it reaches the innermost stable circular orbit $R_{\rm ISCO}$ from where the matter falls into the black hole because it can not continue to orbit closer. If we substitute R_0 for $R_{\rm ISCO}$, we get for non-rotating black holes the accretion luminosity as following

$$L_{\rm acc} = \eta \dot{M}_{\rm acc} c^2, \tag{1.4}$$

where $\eta = 1/12$ is the efficiency of the non-rotating black hole (correct relativistic correction is lower). With a maximally rotating BH, we get the approximate value of $\eta = 1/2$.

We will focus on the accretion disk formed by tidal disruption event (TDE) since this is going to be in our interest later. In the late 1970s theoretic physicists calculated that if a star were close enough to a SMBH, tidal forces would rip it apart. The black hole would accrete part of the star and produce debris with velocities high enough so that the material would escape the gravitational potential of SMBH. The distance where the star would be tidally disrupted by a black hole of mass $\rm M_{BH}$ is given by

$$R_{\rm T} \approx R_* (M_\bullet / M_*)^{1/3} \tag{1.5}$$

where R_* and M_* are the radius and mass of the star. Fig. 1.5 shows a diagram of a shredded star with the trajectory of its debris.

Approximately half of the star's material escapes from the black hole forever and the rest stays gravitationally bound in elliptical orbits and continues spiralling towards the accretion disk around the black hole. The rate at which the stars are disrupted depends on the gravitational scatterings of stars (their density in NSCs). Models predict that only in thousands of years in one particular galaxy, a star undergoes these conditions. Simulations

also show interesting conclusions: the interval between disruption time and peak luminosity of the TDE flare can be used to determine the mass of the SMBH, as $\Delta t \propto M_{\mathrm{BH}}^{1/2}$; the radial density profile of a star immensely impacts the peak luminosity (lower density near the surface slows the rise-to-peak luminosity); we can also see the tidal disruption of giant gas clouds although they are further apart from the black hole (disruption lasts longer, hundreds of years).

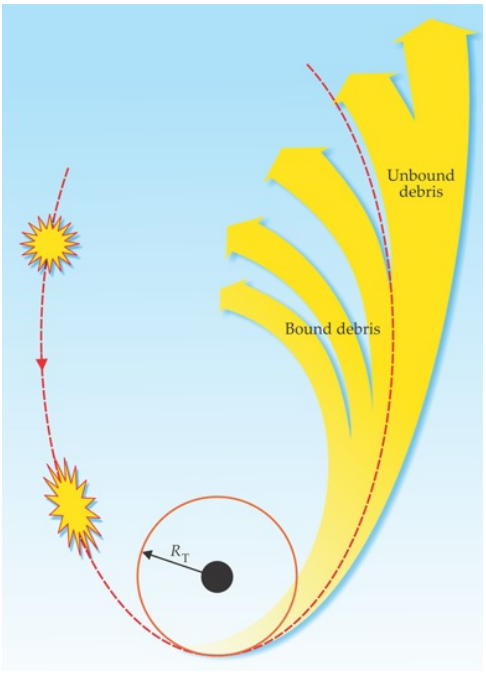

Figure 1.5: Tidal disruption event (Gezari, 2014)

As of right now, we established all the main ingredients of a typical galactic nucleus in active state (i.e. having high energy output). Massive black hole surrounded by an accretion disk and nuclear star cluster are essential elements to the model we meet later.

To complete the picture of a typical galactic nucleus we need to mention two more things. In the gravitational potential dominated by SMBH broad emission lines are created from gas and dust found in the central interstellar medium. These lines have line widths of a few $1000\,\mathrm{km.s^{-1}}$ due to the Doppler-broadening of the ionized gas emission (caused by the motion of small clouds). They are observed in galaxies with a high accretion rate of the order of $1\,\mathrm{M_\odot\,yr^{-1}}$. An important region where gas flows straight towards the SMBH is the region inside the Bondi radius given by

$$r_{\mathrm{Bondi}} \approx \frac{GM_\bullet}{c_{\mathrm{s}}^2} = 1\left(\frac{\mathrm{M}_\bullet}{2\times10^8\mathrm{M}_\odot}\right)\left(\frac{T_{\mathrm{g}}}{10^8\mathrm{K}}\right)^{-1}\mathrm{pc}. \tag{1.6}$$

with c_{s} being the speed of sound and T_{g} the thermal gas pressure. This is the basic estimate of the region where broad emission lines are created, called broad line region (BLR). The size of BLR is also linked to the monochromatic luminosity of the nucleus. From the fact that absorption lines are rare, a flattened structure of the disk is induced.

Most of the emission in the infrared part of the spectrum is reprocessed emission in a dusty environment. The dust occurs in the distance at least 1 pc from the black hole. This dusty region is nearly symmetric and concentrates around the equatorial plane. It creates a shape similar to a toroid with an opening angle of $\approx 30-60$ degrees. From the observations, there is evidence that the torus is rather not homogeneous but clumpy (from many clouds). To give a basic size estimate of this torus we set its inner radius as a dust sublimation radius

$$R_{\text{sub}} = 0.37\left(\frac{T_{\text{sub}}}{1500\,\text{K}}\right)^{-2.8}\left(\frac{L_{\text{AGN}}}{10^{45}\,\text{erg.s}^{-1}}\right)^{1/2}\left(\frac{a_{\text{dust}}}{0.05\,\mu m}\right)^{-1/2}\text{pc}, \tag{1.7}$$

where T_{sub} is the sublimation temperature, L_{AGN} is the AGN luminosity in UV, a_{dust} is the grain size. The outer radius of the torus is approximated to be 5–10 times larger than R_{sub}. The inner radius and opening angle depend on the AGN luminosity. It is established that the inner radius of the torus coincides with the outer radius of BLR. All equations in this chapter are derived in Karas et al. (2021).

1.3 Attempts for Classification of AGN

Not every AGN looks the same: the main distinction is their electromagnetic spectrum. The first classification was chosen according to the radio flux which differs by orders of magnitude for different sources. The ”radio-loud” sources are often connected to powerful collimated jets launching from the poles of the supermassive black hole. We can also classify AGNs according to the presence of broad emission lines. In the absence of these lines together with the surpressed continuum we can conclude that the view into the region inside is blocked by torus (type-II objects). Therefore type-I objects are viewed from above, unobscured by the torus, while type-II objects are observed from the edge. This is called the Fanaroff–Riley classification.

In the Fig. 1.6 classification is depicted containing the main parts of AGN. A black hole in the centre is inside an accretion disk and electron plasma. In the radio-loud cases (10 % of the AGNs) a relativistically moving jet is present. In the broad line region and narrow line region emission lines are created.

We can also add another category of AGN called blazars. They are active galactic nuclei with jets aiming toward us. The SED of blazars is mainly dominated by the emission from the jet. We can also divide blazars into BL Lac objects and Flat-Spectrum Radio Quasars (FSRQ). In FSRQs broad optical emission lines are present while absent in BL Lac objects. This can be explained by accretion mode efficiency.

1.4 Stochastic Fluctuations

The AGN variability is not periodic because it is driven by stochastic processes (”having a random probability distribution or pattern that may be analysed statistically but may not be predicted precisely”) [1]. Our monitoring satellites can also detect quasi-periodic flux density changes. These changes can be caused by an orbiting perturber, i.e. black hole, a neutron star or even a main-sequence star.

If we want to analyze the stochastic mechanism, PSD (power spectral density) is a good place to start. We take the Fourier transform of the light curve $C(t)$ from AGN

$$\tilde{C}(\nu) = \int_{-\infty}^{\infty} C(t)e^{-i2\pi\nu t}, \tag{1.8}$$

[1] Oxford Languages

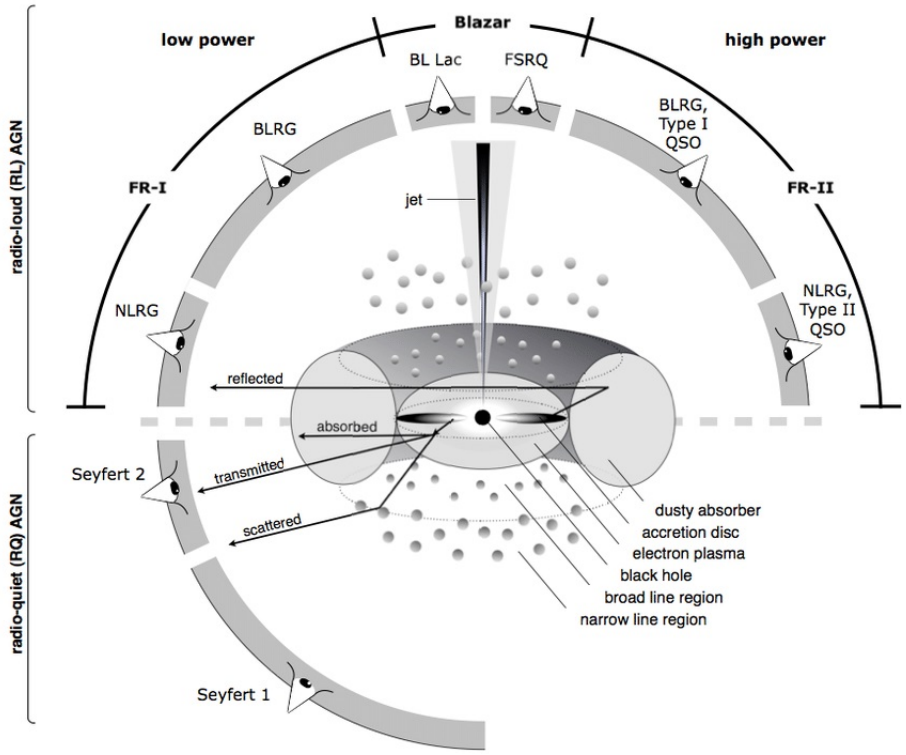

Figure 1.6: Schematic representation of our understanding of the AGN phenomenon. The outlook of AGN depends on the viewing angle. NLRG - Narrow-line radio galaxies, BLRG - Broad-line radio galaxies, QSO - Quasi-stellar objects. Credit: Beckmann and Shrader (2012).

where ν is te frequency. The PSD is just the square of the absolute value of $\tilde{C}(\nu)$. Over a broad frequency range from smallest frequencies to biggest ones (smallest timescales, reversely), PSD is generally described by a broken power-law function that has one or two break frequencies (Fig. 1.7). Without break frequencies the total power obtained by integrating over all frequencies would be infinite and that is not physically possible.

However, we have a hard time observing the frequency breaks. At low frequencies, it is required to have an extremely long monitoring program at hand. For high frequencies, the PSD is hard to capture because of the signal-to-noise ratio limits. The break frequency between $\sim \nu^{-1}$ and $\sim \nu^{-2}$ is observed both for AGN and stellar-mass black holes. The second break between $\sim \nu^{0}$ and $\sim \nu^{-1}$ is mostly associated with stellar-mass black holes.

The characteristic variability timescale $T_{\rm B} = 1/\nu_{\rm B}$ has been determined empirically to be

$$T_{\rm B} \propto \frac{M_\bullet^{1.12}}{\lambda_{\rm Edd}^{0.98}}, \tag{1.9}$$

where $\lambda_{\rm Edd} = L_{\rm bol}/L_{\rm Edd}$ is an Eddington ratio between bolometric luminosity $L_{\rm bol} = = \eta \dot{M} c^2$ and an Eddington accretion rate $L_{\rm Edd} = 4\pi G M_\bullet m_{\rm p} c/\sigma_{\rm T}$. From expressing the Eddington ratio as $\lambda_{Edd} \propto \dot{M}/M_\bullet$ we have a simple law for variability timescale

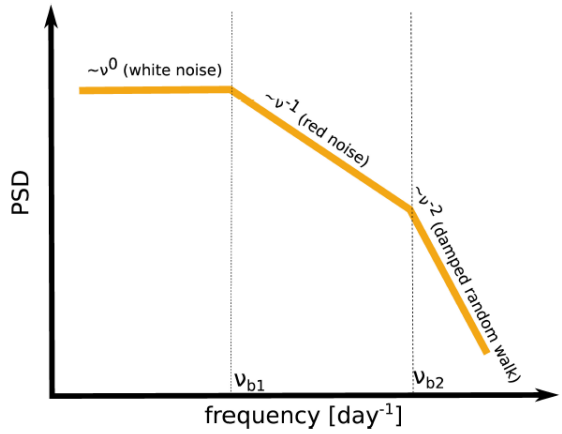

Figure 1.7: Power spectral density being described by a broken power-law function with two breaks. At low frequencies, the PSD is dominated by the 'white'-noise process (PSD is almost independent of the frequency), at high frequencies, the slope is the steepest. The part in the middle is dominated by the 'red'-noise process. Credit: Karas et al. (2021).

$$T_{\mathrm{B}} \sim \frac{M_{\bullet}^2}{\dot{M}}. \tag{1.10}$$

that is true for accreting SMBHs. The variability timescale has been associated with the standard timescales of an accretion disk. Also, the timescale could be determined by the characteristic timescale of the production of hard X-rays.

Introduction to QPEs

Quasi-periodic eruptions (QPEs in short) is a newly discovered category of X-ray variability transients coming to us from galactic nuclei. They are high-amplitude bursts with fast periods ranging from tens of minutes to a few days. These bursts can be detected because their count rate rises by about one order of magnitude above the so-called 'quiescent level' which is associated with relatively efficient accretion flow onto a lighter supermassive black hole (SMBH). Amplitudes of these bursts lie in the soft X-ray part of the electromagnetic spectrum as well as the quiescent radiation. There are 8 main sources of QPEs, as of today, with different variabilities and timing properties.

2.1 Observations

After the first discovery in galaxy GSN 069 (Miniutti et al., 2019), other QPEs have been observed from the nuclei of other galaxies: RXJ1301.9+2747 (Giustini et al., 2020), eRO-QPE1, and eRO-QPE2 (Arcodia et al., 2021), as well as XMMSL1J024916.6-04124 (Chakraborty et al., 2021). In the last source, there are only 1.5 bursts detected (the second burst is measured only in the first half). Although all of its properties fall in the category of QPEs, the origin of this source is still not certain. There is also another QPE candidate from galaxy J023017.0+283603 (Guolo et al., 2024), hereafter Swift J0230+28, that has physical characteristics very similar to previous sources but reveals to us much more new. Swift J0230+28 shows:

1. Extreme irregularities in its QPE periods on the scale of $\approx$ 20 days.
2. Variable ultra-fast outflows that are detected during the rises of eruptions.
3. Transient radio emission.

About two years later, QPEs reappeared in GSN 069 (Miniutti et al., 2023) and we can see two consecutive eruptions separated by a much shorter recurrence time than before. In addition, their intensities and peak temperatures are now remarkably different. The newest discovery includes another two sources observed by eROSITA as well, namely eRO-QPE3 and eRO-QPE4 (Arcodia et al., 2024).

2.2 Physical Properties

To define this new category of X-ray eruptions the best option would be to list common properties of different sources. As its name suggests, 'quasi-periodic' describes something

that displays periodic behaviour but with some deviations. This adjective was chosen to describe the time periodicity or recurrence time of the bursts. In other case, it would be accurate to name them 'quasi-luminous' as well.

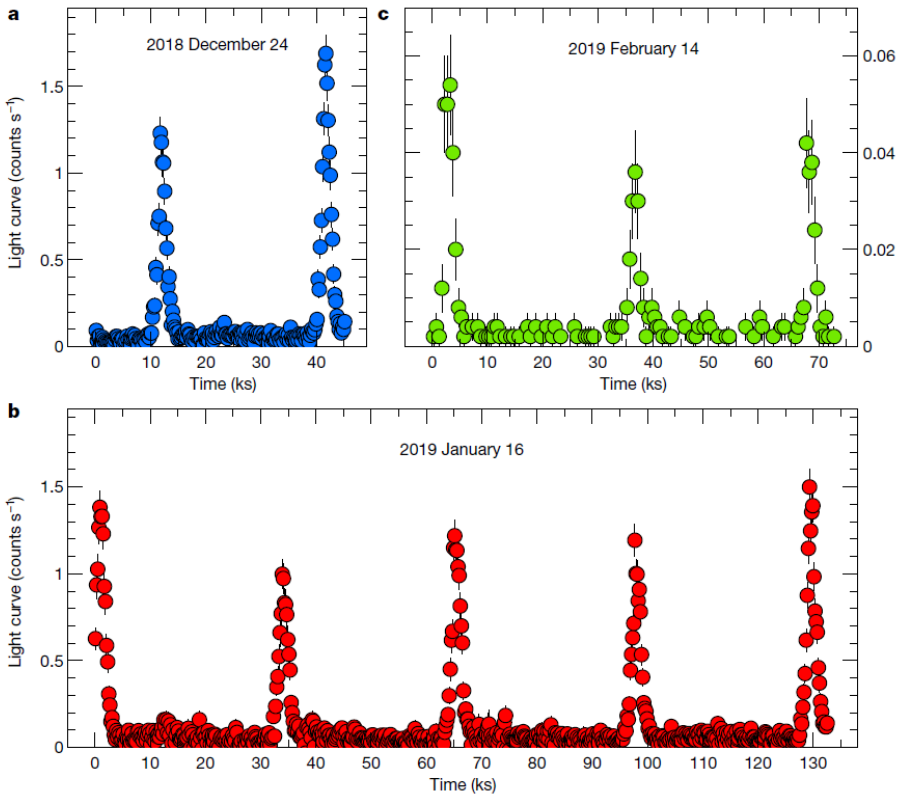

Figure 2.1: X-ray QPEs by XMM-Newton and Chandra. Light curves from December 2018 onwards, a–c. The background-subtracted 0.4–2 keV light curve from the XMM3 (a), XMM4 (b) and Chandra (c) observations. Error bars represent 1σ confidence intervals in all panels. Some of the error bars are smaller than the symbol size. Credit: Miniutti et al. (2019).

During these bursts the X-ray count rate increases by up to two orders of magnitude (depending on the energy band) above the quiescent level. In this quiescent phase, X-ray luminosity is consistent with emission from accretion onto a massive black hole (MBH). Peak X-ray luminosity would be between 10^{42}–10^{43} erg.s^{-1}. QPEs have thermal spectra with temperatures ranging from $kT \simeq 50$–80 eV to $\simeq 100$–250 eV depending on the phase of the cycle.

QPE host galaxies may be classified as low-mass post-starburst galaxies that also correspond to galaxies that experienced TDEs. Both types have a tendency towards low-mass MBHs of 10^{5-7} M$_\odot$. Two QPE sources have been explicitly linked to X-ray TDEs so far (GSN 069 and XMMSL1 J024916.6-04124).

In the following subsections, we are going to list all QPE sources observed up to date with their light curves and basic properties.

2.2.1 GSN 069

From December 2018 onwards, the galactic nucleus of GSN 069 exhibited X-ray luminosity with high amplitude and short timescale variability. During 54 days of observations, 9 bursts were detected by satellites XMM-Newton and Chandra. Observed light curves are in Fig. 2.1. Interestingly enough, no bursts were observed in a long XMM-Newton exposure (83 ks) on 2014 December 5.

During these eruptions, the X-ray count rate increases by up to two orders of magnitude with an event duration of an hour and a recurrence time of about 9 hours. From there the duty cycle would be approximately 6%. Eruptions are associated with fast spectral transitions between a cold and a warm phase in the accretion flow around a massive black hole (of approximately $M_{\rm BH} = 10^5 {\rm M}_\odot$) with peak X-ray luminosity of about $L_{\rm x} = 5 \cdot \cdot 10^{42}\,{\rm erg.s}^{-1}$. The warm phase has kT (where T is the temperature and k is the Boltzmann constant) of about 120 electronvolts.

The relative QPE amplitude is heavily dependent on the energy band as we can see in Fig. 2.2. Maximum amplitude of $\simeq$ 100 is in the 0.6–0.8 keV band while in the 0.2–0.3 keV band is about 2.

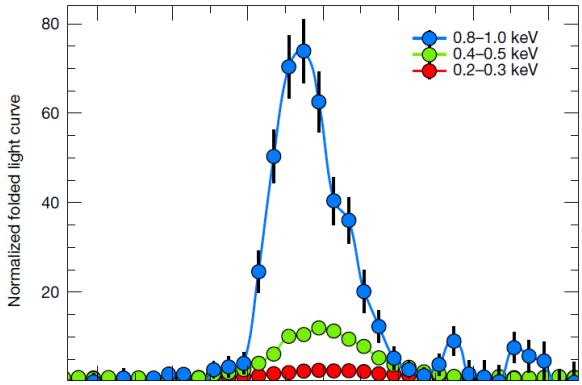

Figure 2.2: The QPE energy dependence from the longest XMM4 observation. We show normalized light curves with respect to their quiescent level to highlight the energy dependence of the amplitude. Credit: Miniutti et al. (2019).

During QPE, while X-ray spectrum oscillates between cold ($\simeq$ 50 eV) and warm phase ($\simeq$ 120 eV), the $L \propto {\rm T}^4$ relation is valid only for the quiescent level emission. During the eruption, this is broken so the spectral evolution can not be explained by the change of mass accretion rate. The thermal-like emission could be associated with the Comptonization of the lower-energy disk photons in a warm, optically thick corona.

After two years of silence, XMM-Newton detected a completely new phase of QPEs from GSN 069. Two consecutive bursts were seen separated by a much shorter period than before and their amplitude was different as well. The EPIC pn, MOS1, and MOS2 0.2–1 keV light curves during the new XMM-Newton observation (XMM12) are displayed in Fig. 2.3.

There is one weak and one strong peak separated by $\simeq$ 20 ks which is a shorter recurrence time than in previous phase ($\simeq$ 32 ks).

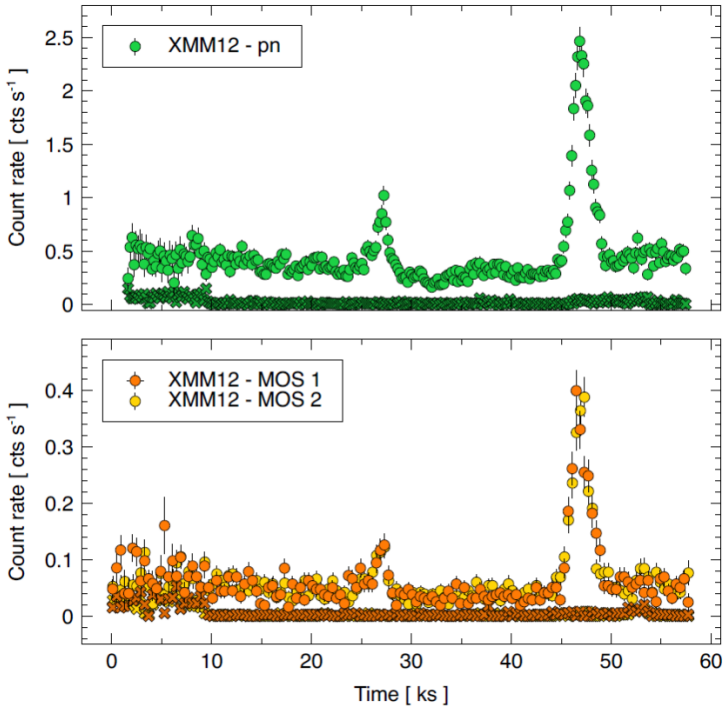

Figure 2.3: EPIC and MOS light curves. Background light curves are also shown to highlight that they are different during initial exposures. Credit: Miniutti et al. (2023).

2.2.2 RX J1301.9+2747

In June 1991, a rapid flare lasting more than 2 ks with different X-ray count rate compared to the average value was detected by ROSAT. RX J1301.9+2747 was observed also in December 2000 and 2009. It is an ultra-soft X-ray source that was fitted by a thermal-disk component with kT $\sim$ 30–50 eV in the low-flux regime and with kT $\sim$ 100–300 eV in the high-flux regime. Black hole mass is estimated on $M_{BH} \sim 0.8\text{–}2.8 \cdot 10^6 M_\odot$. After those detections another observation was made by XMM-Newton in 2019.

The light curves are in Fig. 2.4.

2.2.3 eRO-QPE1 and eRO-QPE2

After a systematic search of half of the X-ray sky SRG/eROSITA was successful in finding another variable source changing on small timescales. After processing the data it showed a strong signal of a very soft X-ray spectrum consistent with a thermal black-body emission. eROSITA showed peak luminosity of $\simeq 9.4 \cdot 10^{42}$ erg.s^{-1} in the 0.5–2 keV part of the spectrum. Follow-up observations included the XMM-Newton satellite observing three consecutive bursts. To better characterize the eruptions, NICER observation started on ISS and revealed 15 more eruptions in 11 days (Fig. 2.5).

The second observation with eROSITA (we call it eRO-QPE2) showed something similar in another galaxy. The resulting QPE luminosity in the 0.5–2 keV band was approximately $1.0 \cdot 10^{42}$ erg.s^{-1}. Follow-up observation with XMM-Newton showed us 9 eruptions in only one day (Fig. 2.6).

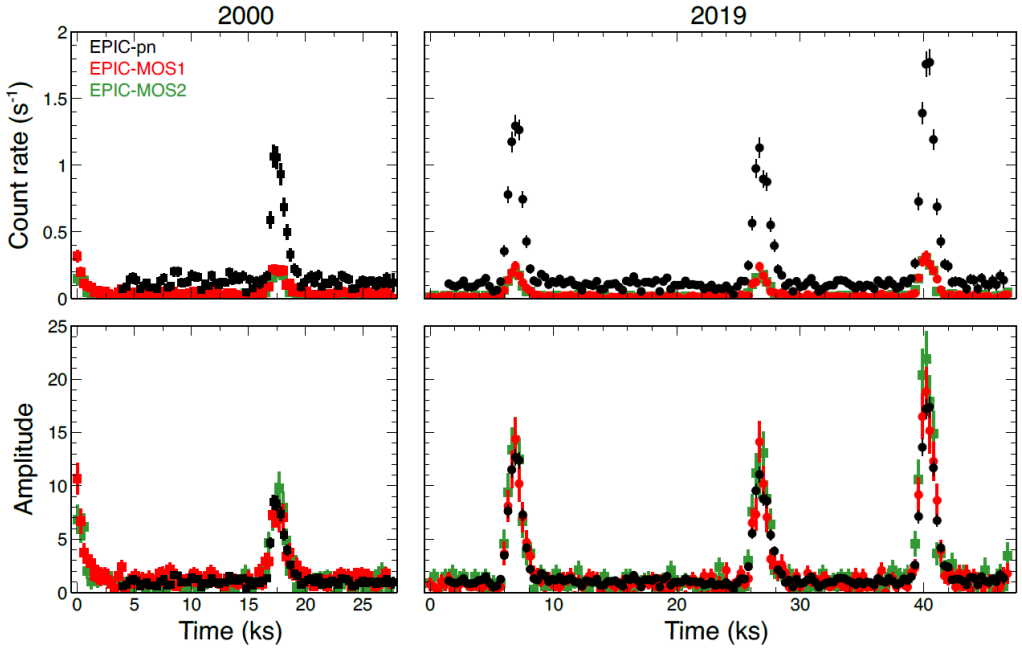

Figure 2.4: Background-corrected light curves of RX J1301.9+2747 in the 0.2–2 keV band. In the bottom panels, the count rates have been normalised to the quiescent level. Credit: Giustini et al. (2020)

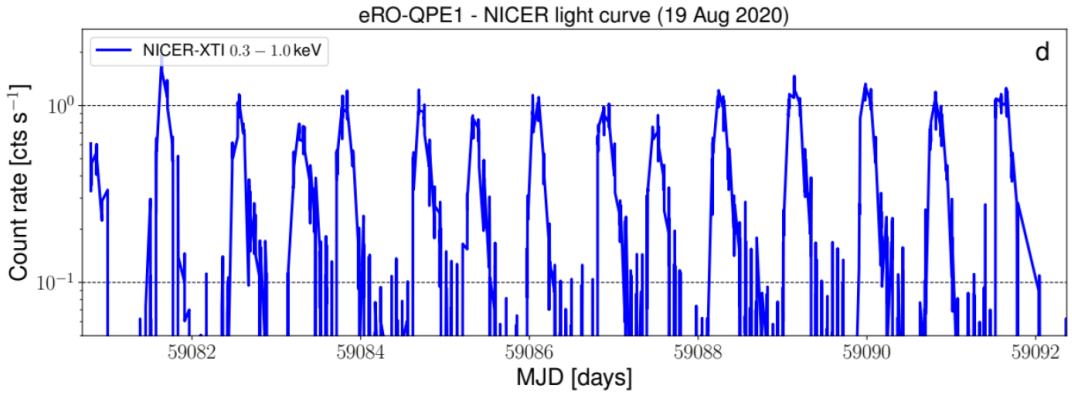

Figure 2.5: Background subtracted NICER-XTI light curves, first eROSITA QPE. The mean rise-to-decay duration is $\sim$ 7.6 hours and mean recurrence time $\sim$ 18.5 hours. Credit: Arcodia et al. (2021).

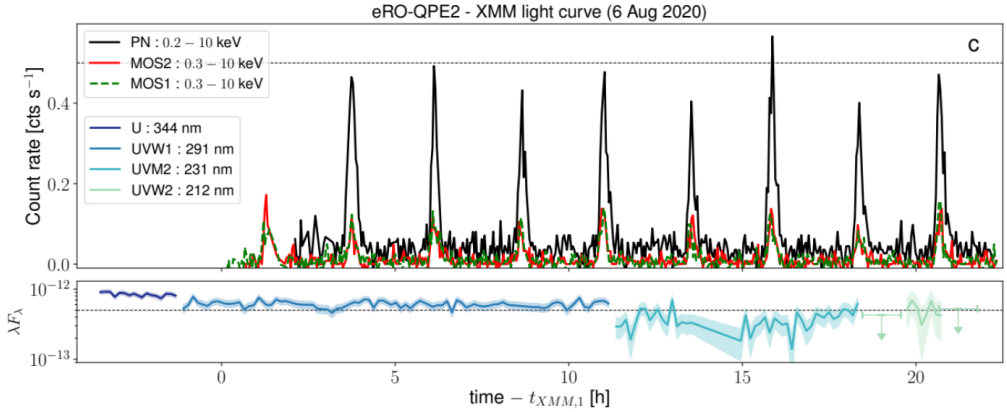

Figure 2.6: Background subtracted XMM-Newton light curves, second eROSITA QPE. The start of the exposure is MJD∼59067.846, the mean of rise-to-decay duration is ∼ 27 minutes, and the peak-to-peak separation ∼ 2.4 hours. Credit: Arcodia et al. (2021)

We can see that eRO-QPE1 and eRO-QPE2 are different from each other as the recurrrence times and X-ray luminosity are both one order of magnitude longer for the eRO-QPE1. It is also important to note that the peak X-ray luminosity of eRO-QPE1 is the most extreme out of all QPE sources.

But they also share physical properties. For example, both observations show no evidence of optical/UV variability which is common for QPEs in general. In the optical part of the spectrum, no broad emission lines are observed suggesting the presence of hot dust (so-called torus).

The galaxy of eRO-QPE1 is not showing any significant emission line so it is classified as passive. On the other hand, strong emission lines of eRO-QPE2 characterize it as a star forming galaxy.

2.2.4 Swift J0230+28

Swift J0230+28 was identified as a part of Swift's live catalog of transients. This area of the sky was first observed by Swift X-Ray Telescope (XRT) between December 2021 and January 2022 and no X-ray emission was detected. Suddenly an observation made on 22 June revealed the brigtening of a factor ∼ 40 with luminosity $2 \cdot 10^{42}\,\mathrm{erg.s^{-1}}$. At first, this event was regarded as a flare from the tidal disruption of a star by a MBH.

During longer monitoring time between June and August of 2022 Swift (XRT) revealed several eruptions that were separated by relatively large time intervals (days) and their duration was also in days. As it was with other so far known QPE sources this one had also no optical/UV variability. Amplitudes of eruptions reach as high as $6 \cdot 10^{42}\,\mathrm{erg.s^{-1}}$ with a relative factor of 100.

In eight months Swift J0230+28 showed us only ten eruptions but the last ones were shorter in duration and also weaker. Light curves in this QPE source are much more variable than ever before, as can be seen in Fig. 2.7.

The position observed by XRT is the same as for the nucleus of a spiral galaxy at 165 Mpc distance. This galaxy did not show any variability in X-ray or radio before. Also,

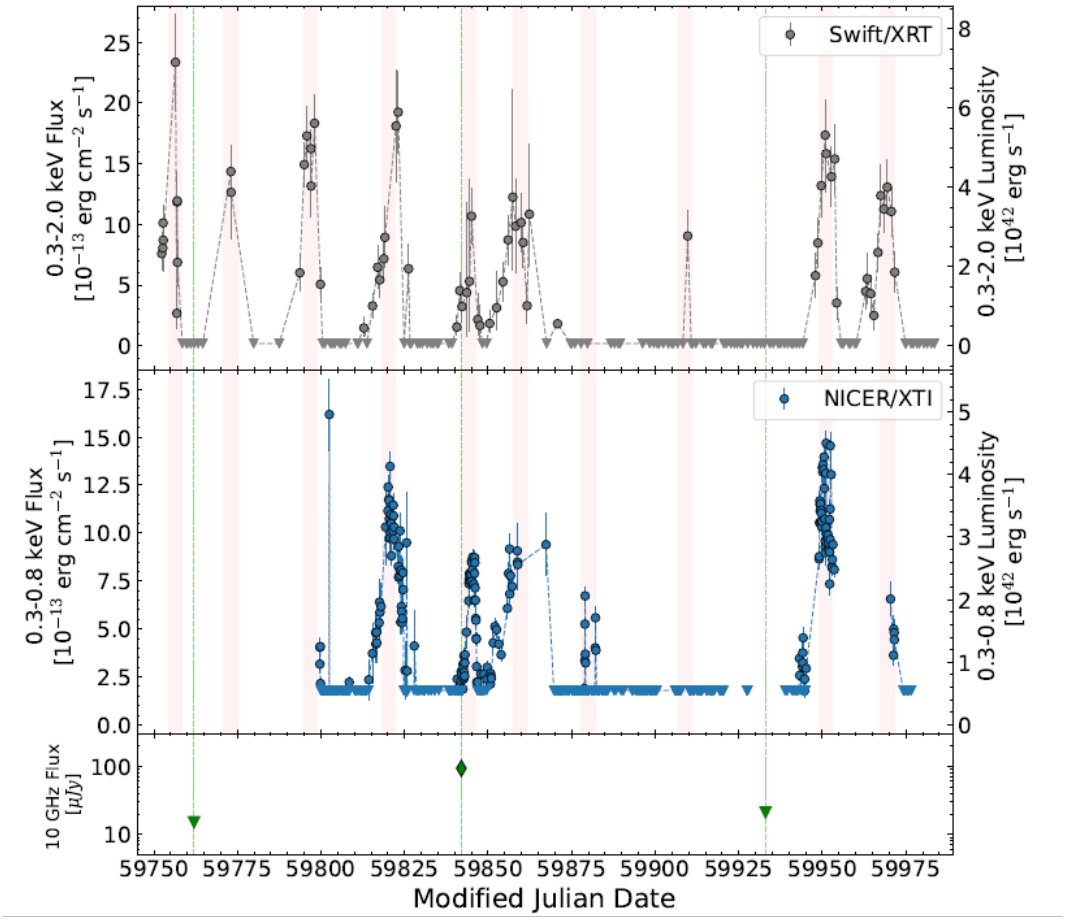

Figure 2.7: Light curves of Swift J0230+28. Top: Swift/XRT 0.3-2.0 keV flux and luminosity light curves. Middle: NICER 0.3-0.8 keV flux and luminosity light curves. No quiescence level was detected, only the upper limit was inferred. In both X-ray panels, circles are detections, reverse triangles are 3σ upper limits of non-detections, and shaded pink regions indicate the peak of the eruptions. Bottom: Radio VLA observations are shown in green diamond (detection) and inverse triangles (non-detection upper limits), green dashed lines mark the epochs of the radio observations for reference. Credit: Guolo et al. (2024).

no variability in IR bands could imply the presence of a dusty torus. From diagnostics of nuclear spectra, there is a possibility that this is the case of weak AGN (LLAGN → low-luminosity AGN). Measuring of the stellar population velocity dispersion (σ_*) was also very useful since it provided us with an estimate of the central black hole mass from the standard $M_{BH} - \sigma_*$ relation. The result is $\log(M_{BH}/M_\odot) = 6.6 \pm 0.4$.

As we now placed Swift J0230+28 in the new QPE category it is now a good time to state the uniqueness of this source since it plays its game on different orders of magnitude. Time separations between peaks are ~ 25 times longer than the longest QPE so far, they are in tens of days. Another interesting feature of Swift J0230+28 is a transient point-like source in its position in radio monitoring. This detection correlates with the eruption times.

2.2.5 eRO-QPE3 and eRO-QPE4

The eROSITA X-ray telescope had another successful observation in 2022 as two new galaxies with QPEs in their nucleus were discovered. Then followed XMM-Newton, NICER, Swift-XRT, SALT, and ATCA. With XMM-Newton two observation windows were performed in July and August 2022 for eRO-QPE3 and one in March 2023 for eRO-QPE4.

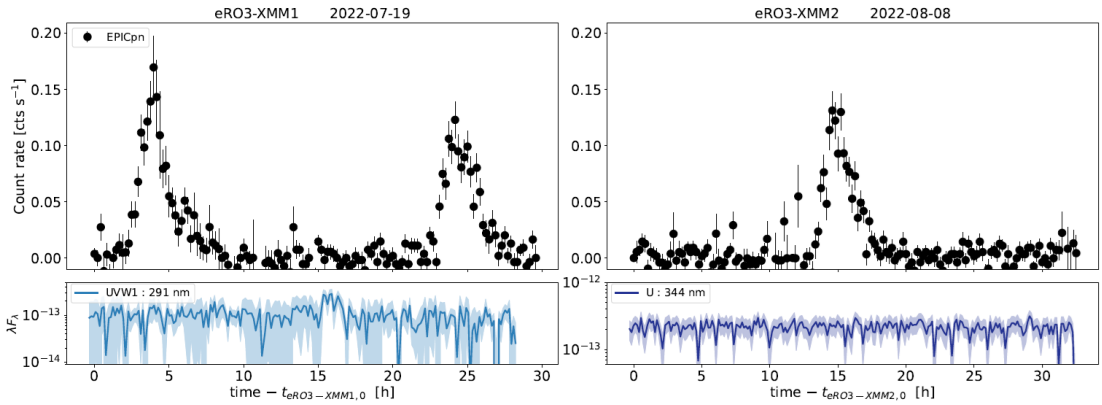

Figure 2.8: XMM-Newton 0.2–10.0 keV EPICpn light curve of eRO-QPE3. First (eRO3-XMM1, left) and second observation (eRO3-XMM2, right). Here, $t_{eRO3\text{-}XMM1,0}$ corresponds to MJD∼59779.799 and $t_{eRO3\text{-}XMM2,0}$ to∼59799.745. Credit: Arcodia et al. (2024).

With eRO-QPE3 two eruptions were caught with a separation of ~ 20.4 h (Fig. 2.8). However, the quiescence level is too weak to be discerned from the background noise. From a disk spectrum that was adopted to model the flux, the soft X-ray luminosity is constrained by $1.6 \cdot 10^{40}$ erg.s^{-1}. After dividing the first eruption into five epochs (rise1, rise2, peak, decay1, decay2), as is common with QPE fitting, the results are: kT_{QPE} = 111 eV and $L_{0.2\text{–}2\,keV} = 4.2 \pm 0.4 \cdot 10^{41}$ erg.s^{-1}. Relative QPE amplitude is therefore 25–30 times brighter than the quiescence flux. The OM UVW1 (U) filter was used with a series of ~ 4400 s-long exposures. The subpanels of Fig. 2.8 show the OM light curves in the respective filters. No variability is there.

With eRO-QPE4 three eruptions are observed. They are closer to each other (9.8 and 14.7 hours) and more symmetric so a Gaussian model can be used to fit them. After adding Comptonisation into the model this yields a disk temperature $kT_{disk} = 43\,eV$ with $L_{0.2–2\,keV} = 1.7 \cdot 10^{42}\,erg.s^{-1}$. Similarly, as before, after dividing eruptions into epochs we can draw quantitative conclusions for properties of the bursts: temperature $kT_{QPE} = 123\,eV$ with $L_{0.2–2\,keV} = 2.9 \cdot 10^{43}\,erg.s^{-1}$. In the OM UVW1 filter no variability is detected again.

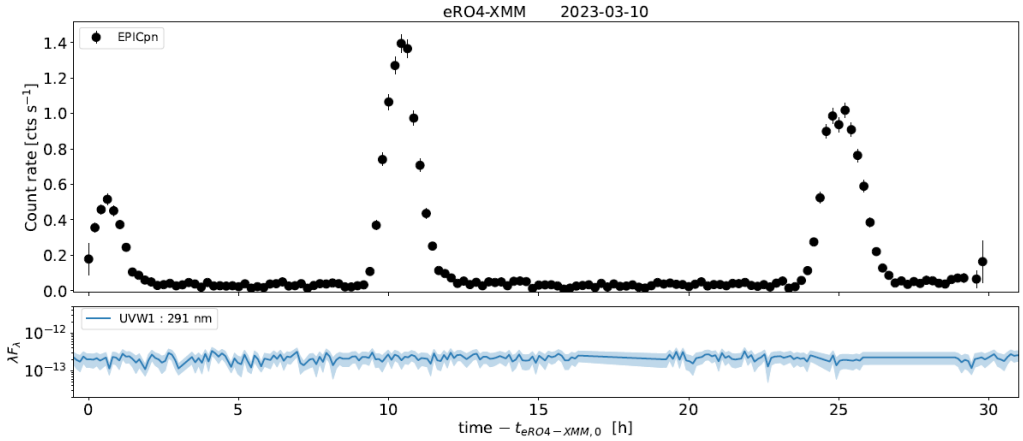

Figure 2.9: XMM-Newton 0.2 - 10.0 keV EPICpn light curve of eRO-QPE4. Here, $t_{eRO3-XMM1,0}$ corresponds to MJD∼60 013.127. Credit: Arcodia et al. (2024)

There are also detections with NICER showing similar results. Average fluxes of maximum bursts are stronger than in the XMM-Newton case. This would suggest long-term decay of peak flux and temperature. This is valid for both eRO-QPE3 and eRO-QPE4.

Swift satellite did not formerly detect eRO-QPE3 but eRO-QPE4 count rates and fluxes of the bursts agree with previous observations. No radio emission was observed at these locations suggesting lower activity of the galactic nucleus than normal AGN would cause.

2.3 Theoretical Models

There is a lot of proposed theoretical models that are trying to explain the mechanism of QPE origin. Some of them are based on disc instabilities (Pan et al., 2022), (Kaur et al., 2022), etc., gravitational lensing (Ingram et al., 2021), etc. But most of them are considering either mass transfer from one or more bodies (King, 2022), (Krolik and Linial, 2022), (Linial and Sari, 2023), etc., and collisions between a secondary object orbiting MBH and accretion disc around it (Metzger et al., 2022), (Linial and Metzger, 2023), etc.

Although some models can explain most of the features of individual QPEs, they are not applicable to all sources. The variety of light curves does not allow a single model to reproduce the light curves even approximately.

2.3.1 Extreme Mass Ratio Inspirals (EMRIs)

Among many models trying to explain the origin of QPEs, this one has a star orbiting a MBH. In order for the energy of individual QPE light curves to be released, pericentre distance of the star has to be in vicinity of partial tidal disruption radius so that its matter can be extracted through extreme tides.

Collisions between a secondary body and accretion flow

As a concrete example, we name an article named *EMRI + TDE = QPE* (Linial and Metzger, 2023). In it a main sequence star that is close to a galactic nucleus as an extreme mass ratio inspiral (EMRI) creates observed light curves in QPE sources (compared to GSN 069 and eRO-QPE2). It goes twice per orbit through an accretion disk of lighter SMBH on a nearly circular orbit (with semimajor axis r_0 and eccentricity e) and ejecting gas clouds above and below the accretion disk plane. In ejected optically thick gas the QPE emission is created by photon production and is harder than the blackbody temperature. This is important because we can detect the eruptions coming out of the softer quiescent disk spectrum. The inner regions of the disk are behind the soft quiescent emission detected between the bursts. The key thing for this mechanism to be understood by the reader is the scheme picture in Fig. 2.10.

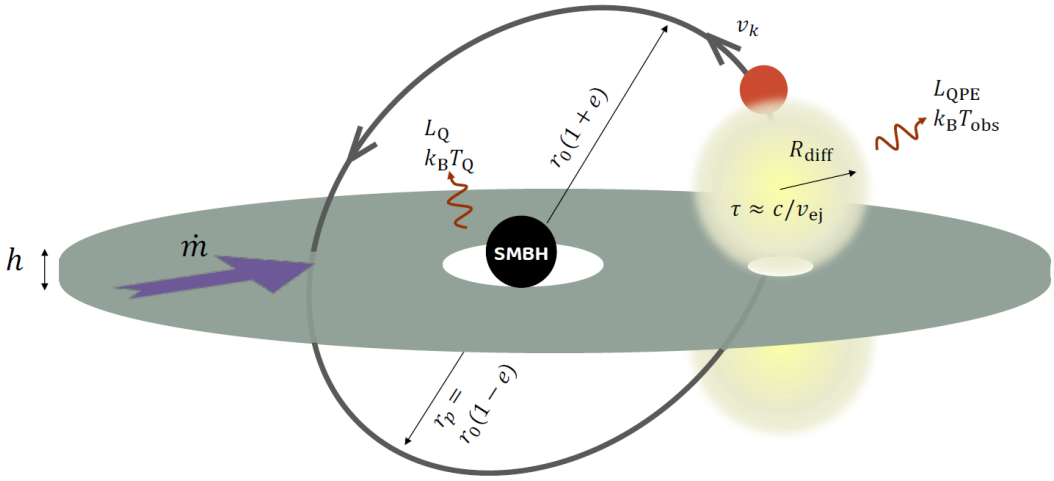

Figure 2.10: Schematic view of our model. A star that orbits a SMBH which is accreting matter through a thin disk of height h at a rate $\dot{m}$. As the ejected material expands and cools down the peak in luminosity can be seen when the optical depth drops below $cv_{\rm ej}$, where $v_{\rm ej} \sim v_{\rm K}$ is the velocity of ejecta caused by the star causing the impact. Orbital velocity of the star is $v_{\rm K}$, therefore $R_{\rm dif} = t_{\rm QPE} v_{\rm K}$ is the cloud radius of the diffused material. Credit: Linial and Metzger (2023).

A stellar mass-transfer model for the radiation

Another example of an EMRI model can be article (Krolik and Linial, 2022) in which a main-sequence star orbits around a SMBH on a slightly eccentric orbit (e = 0.1–0.5). It

transfers its mass to the Roche lobe of the BH (Fig. 2.11) causing relativistic shocks close to the BH that produce thermal X-ray spectrum in the gas going away from the shock. Fluctuations in the recurrence times and duty cycles are created by strong irradiation of the star. This is related to the magnetic fields present in the system.

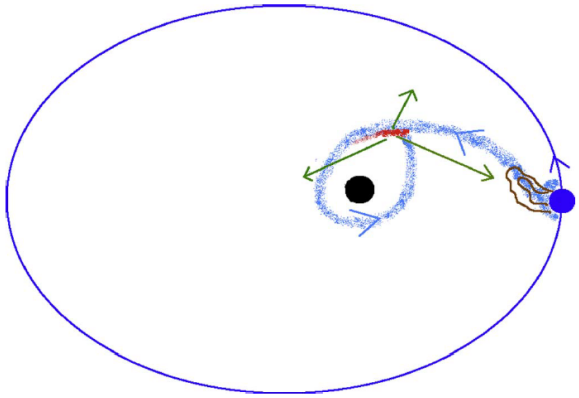

Figure 2.11: Schematic mass transfer. Blue circle (the star) goes around a SMBH on eccentric orbit. In the pericentre its atmosphere expands towards the black hole with the inspiralling material causing flares. Brown curves are magnetic field lines pertruding the material. The material follows eccentric orbit around the black hole and when meets the new inspiralling material it creates shocks (red color) and emits X-rays (green). Credit: Krolik and Linial (2022).

2.3.2 Accretion Disk Instabilities

Disk warping

Formation of accretion disks around black holes is inevitable; the matter has angular momentum and it cannot get easily rid of it. Misalignment of the disk plane to the plane of the black hole spin can cause warping of the disk due to Lense-Thirring precession (most significant for the supermassive black holes). Strongly warped disks can become unstable and undergo breaking into discrete rings that precess almost independently.

When two neighboring rings precess, the angle of their misalignment can oscillate (up to twice the initial angle to the black hole spin vector). They also produce more complicated accretion flow and eventually light curves. The variability timescale of the accretion flow can be on very short timescales (minutes), as well as on the order of months, depending mainly on the warp amplitude and mass accretion rate (Raj and Nixon, 2021).

In Fig. 2.12 a disk structure is shown that produces light curves with a recurrence period of $\sim$3.5 h with 0.4–2 keV flux increased by a factor of 10–100 in approximately one hour.

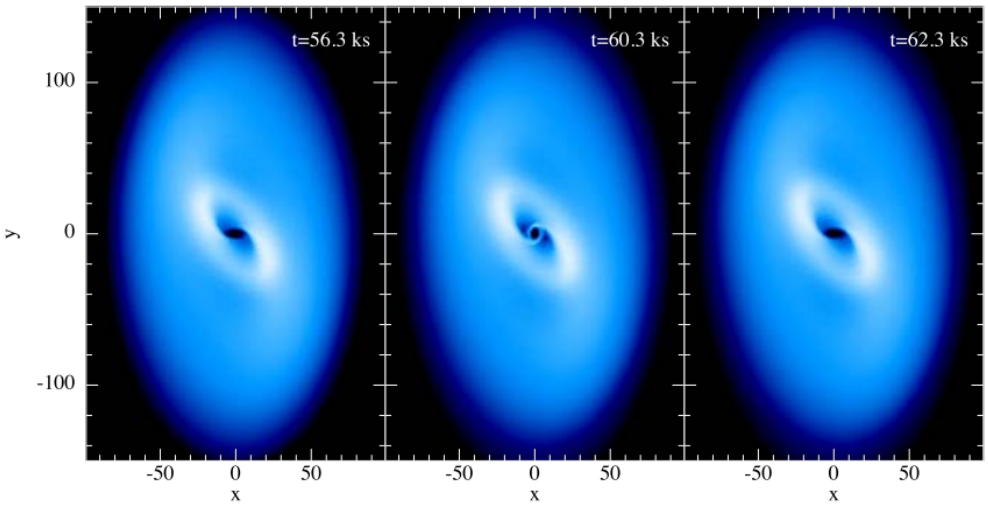

Figure 2.12: Disk structure is shown before, during, and after a peak in accretion rate. Axes are shown in the units of gravitational radii. White regions show the highest column densities and dark blue the lowest. Here we have a MBH of $4 \cdot 10^5 M_\odot$ in the middle. Credit: Raj and Nixon (2021).

Model of Perturber Crashing with an Accretion Disk

In this section, we choose a specific theoretical model that is trying to explain the physical nature of QPEs. We simplify it and model light curves for different QPE sources we have data on. This model comes from the article Franchini, Alessia et al. (2023).

3.1 Original Article

In this model, QPEs are produced by extreme mass ratio inspiral (EMRI). This is a binary in which the lighter companion (in this case a black hole BH) adiabatically inspirals onto a MBH undergoing gravitational wave emission. The X-ray bursts are created whenever the companion crosses an accretion disk. We consider the precession of the disk around the MBH with relativistic Lense-Thirring precession. Also, apsidal and nodal precession of the EMRI companion are included. All precessions together are accountable for the quasi–processes like periodicity or luminosity fluctuations.

The parts of the system are: MBH with mass M_1 and spin parameter χ that is inside a precessing accretion disk and its properties are compatible with a disk generated by a stellar TDE (as we will see later). Around the MBH a stellar–mass BH companion orbits with mass M_2 and can cross the accretion disk up to three times per orbit. We can imagine the system in Fig. 3.1.

3.1.1 Post-Newtonian Trajectory of the EMRI

The key thing to take into account is the equation of motion of the EMRI system

$$\frac{\mathrm{d}^2\mathbf{r}}{\mathrm{d}t^2} = -\frac{GM}{r^2}\Big((1+\mathscr{A})\mathbf{n}+\mathscr{B}\mathbf{v}\Big)+C_{1.5}+\mathscr{O}(\frac{1}{c^8}) \tag{3.11}$$

where: $\mathbf{r}$ is the relative separation and $\mathbf{v}$ the velocity of the EMRI components, $\mathbf{n} = \mathbf{r}/|\mathbf{r}|$, M is the binary mass, and the G the gravitational constant. The parameters take into account effects for GW emission and the effect of the MBH spin (spin-orbit coupling).

3.1.2 Disk Model

Here, a disk formed by a TDE of a star is considered because there is now evidence that QPEs are successors of the tidal disruption events. The disk reaches right into the innermost circular orbit (ISCO) which is a function of the primary BH spin χ. We also

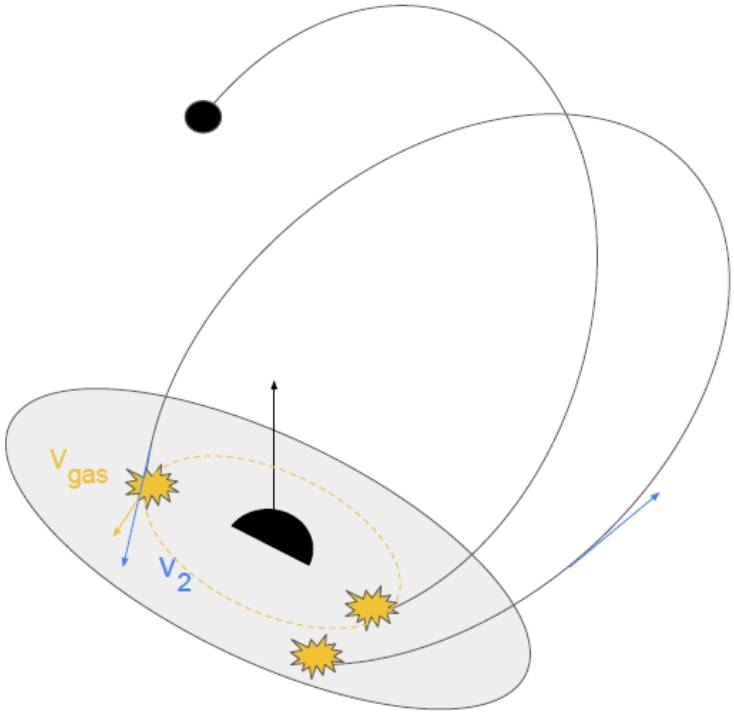

Figure 3.1: Schematic picture of the system. The big central sphere in the middle is the primary MBH being orbited by smaller BH (secondary). The disk is in grey and every time the secondary crosses it a lot of disk material in the impact area gets shocked. The spin of the primary is noted by an arrow. Blue and yellow vectors represent the velocities of the secondary and the gas respectively. Credit: Franchini, Alessia et al. (2023).

assumed that the disk is prograde to the spin of the MBH. It has mass of $M_{\rm d} = fM_{\odot}$ where f is considered not to be bigger than 4. The mass is distributed with a power-law surface density profile $\Sigma = \Sigma_0 (R/R_{\rm g})^{-p}$ all the way into $R_{\rm out} = 200$–$400\,R_{\rm g}$. $R_{\rm g} = GM_1/c^2$ is the gravitational radius.

We also need to normalize the surface density profile by

$$\Sigma_0 = \frac{M_{\rm d}(2-p)}{2\pi R_{\rm g}^2}\left(\left(\frac{R_{\rm out}}{R_{\rm g}}\right)^{2-p} - \left(\frac{R_{\rm ISCO}}{R_{\rm g}}\right)^{2-p}\right), \tag{3.12}$$

where p is the power law index. We define the disk aspect ratio as a ratio of its height to its radius

$$\frac{H}{R} = \frac{3}{2}(2\pi)\eta^{-1}K(R)^{-1}\dot{m}_1\left(\frac{R}{R_{\rm g}}\right)^{-1}, \tag{3.13}$$

$$K(R) = \frac{1}{2} + \left[\frac{1}{4} + 6\left(\frac{\dot{m}_1}{\eta}\right)^2\left(\frac{R}{R_{\rm g}}\right)^{-2}\right]^{1/2}. \tag{3.14}$$

The $K(R)$ coefficient deals with the different structure of a slim disk. Here, $\eta = 0.1$ is the efficiency of accretion, and $\dot{m}_1 = \frac{\dot{M}_1}{\dot{M}_{1,\rm Edd}}$ determines the accretion rate of the MBH normalised to its Eddington limit.

Under other physical assumptions mentioned in the source, the disk is meant to precess rigidly with a frequency $\Omega_{\rm p}$ that denotes the angular momentum weighted average of the Lense-Thirring precession $\Omega_{\rm LT}(R)$ frequency

$$\Omega_p = \frac{\int_{R_{\rm ISCO}}^{R_{\rm out}} \Omega_{\rm LT}(R) L(R) 2\pi R {\rm d}R}{\int_{R_{\rm ISCO}}^{R_{\rm out}} L(R) 2\pi R {\rm d}R} \tag{3.15}$$

where angular momentum is $L(R) = \Sigma\Omega(R)R^2$. Lense-Thirring frequency is given by:

$$\Omega_{\rm LT}(R) = \frac{c^3}{2GM_1} \frac{4\chi\left(\frac{R}{R_{\rm g}}\right)^{-3/2} - 3\chi^2\left(\frac{R}{R_{\rm g}}\right)^{-2}}{\left(\frac{R}{R_{\rm g}}\right)^{-3/2} + \chi}. \tag{3.16}$$

The gas orbits the MBH on a circular Keplerian orbit, so the gas orbital velocity modulus and frequency are $v_{\rm gas}$(R) = $\sqrt{GM_1/R}$ and $\Omega(R) = \sqrt{GM_1/R^3}$, respectively.

3.1.3 Disk Crossing

The companion crosses the disk between one and three times per orbit and the crossing can happen at pericentre anywhere along the precessing disk line of nodes. The apsidal and nodal precession of the EMRI companion further complicate this and the interval between subsequent crashes changes.

The disk is represented by a rigidly rotating plane that does not influence the evolution of EMRI. Firstly, we have to calculate the times and places where the companion crosses the disk plane. Geometrically that corresponds to a relation $w_x x_2 + w_y y_2 + w_z z_2 = 0$, where **r** = (x_2, y_2, z_2) is the position vector of M_2 and **w** = (w_x, w_y, w_z) is the normal of the disk plane. But, the disk plane changes with time because of the precession:

$$w_x = \sin(\Omega_{\rm p} t)\sin(i_{\rm disk}), \tag{3.17}$$

$$w_y = \cos(\Omega_{\rm p} t)\sin(i_{\rm disk}), \tag{3.18}$$

$$w_z = \cos(i_{\rm disk}). \tag{3.19}$$

The relative velocity vector between the gas in the disk and M_2 is given by a vector difference $\mathbf{v}_{\rm rel}$ = $\mathbf{v}_{\rm gas}$ - $\mathbf{v}_2$, where the gas velocity in the reference plane of the disk is given by:

$$\mathbf{v}_{\rm gas,d} = \sqrt{\frac{GM_1}{R_{\rm cross}}}(-\sin\phi_{\rm d}, \cos\phi_{\rm d}, 0) \tag{3.20}$$

where $R_{\rm cross}$ is the crossing radius and $\phi_{\rm d} = \arctan\left(y_{2,{\rm d}}/x_{2,{\rm d}}\right)$ is the polar angle in the reference plane. We assume that the crossing is short enough so that the relative velocity does not change.

The crossing times we can determine by the procedure above are valid for the EMRI system reference frame. But we also need to find out the correlation between that and the times when we see the bursts from the crossings. While the photons from the EMRI crossing are released they travel to the observer and are influenced by the light travel time

within the binary system (Roemer delay $\Delta_R(\tau)$), the non-zero curvature created by the primary that bends the travel path (Shapiro delays $\Delta_S(\tau)$ and Einstein delays $\Delta_E(\tau)$). The expressions for delay are in the article.

3.1.4 Emission

We consider the emission from a cloud of gas that comes out of the disk as a consequence of the crossing of the EMRI companion. The cloud has an initial radius comparable to the influence radius of the secondary object:

$$R_{\rm in} \sim R_{\rm inf} = \frac{GM_2}{c_{\rm s}^2 + v_{\rm rel}^2}, \tag{3.21}$$

where $c_{\rm s}$ is the speed of sound in the disk and v_{rel} is the modulus of the relative velocity. The cloud is considered to be optically thick with a post-shock temperature $\sim 10^6$ K that corresponds to the observed QPE emission of $\sim$ 100–120 eV. The exact value of the post-shock temperature is determined by using the Rankine-Hougoniot condition for shocks in a pressure-dominated gas disk:

$$T_2 = \left[1 + \frac{8}{7}(\mathscr{M}_{e,1}^2 - 1)\right]^{1/4} T_1 \tag{3.22}$$

where T_1 is the pre-shock disk gas temperature and $\mathscr{M}_{e,1}$ is the effective pre-shock Mach number:

$$\mathscr{M}_{e,1} = \left(3\gamma \frac{\mathscr{M}_1^2}{4R_{\rm p}}\right)^{1/2}, \tag{3.23}$$

where $\mathscr{M}_1 = v_{\rm rel}/c_{\rm s}$ is the Mach number, $R_{\rm p}$ is the ratio between the radiation and gas pressure before the shock, $\gamma = 4/3$ is the adiabatic index. From the relation connecting the total pressure to the gas sound speed we can determine pre-shock temperature T_1:

$$P = P_{\rm rad} + P_{\rm gas} = \frac{\rho c_{\rm s}^2}{\gamma}. \tag{3.24}$$

The pressure components are given by:

$$P_{\rm rad} = \frac{4}{3}\frac{\sigma_{\rm sb} T_1^4}{c} \tag{3.25}$$

$$P_{\rm gas} = \frac{\rho k_{\rm B} T_1}{m_{\rm p}\mu} \tag{3.26}$$

while $\sigma_{\rm sb}$ is the Stefan-Boltzmann constant, $k_{\rm B}$ is the Boltzmann constant, $\mu = 1$ being the mean molecular weight and $m_{\rm p}$ the proton mass.

The cloud is expected to emit black body radiation and it adiabatically expands after leaving the dense accretion disk. QPEs can also be detected when their peak temperature T_2 is significantly higher than T_1. From our data, the ratio of these is normally $T_2/T_1 \approx$ 2–3. From these we can infer linear growth of the adiabatic expansion of the ejected cloud:

$$R(t) = R_{\text{in}} + \frac{2R_{\text{in}}}{\Delta t_{\text{QPE}}} t, \tag{3.27}$$

where Δt_{QPE} is the duration of the QPE. Therefore the QPE starts at the time of the secondary impact and the temperature changes in time as $T_{\text{exp}} = T_2(R_{\text{in}}/R(t))$.

The emitted luminosity in the X-ray band of 0.2–2 keV is then:

$$L_{\text{x}} = 4\pi R(t)^2 \int_{0.2\,\text{keV}}^{2\,\text{keV}} \frac{2h\nu^3}{c^2} \frac{\mathrm{d}\nu}{e^{\frac{h\nu}{k_{\text{B}}T_{\text{exp}}}} - 1} \tag{3.28}$$

Emission starts at the time of the impact. For different sources, we assign a different time length of the QPE duration (different for each burst in a given source as well) and an amplitude.

3.1.5 Secondary Object

As long as the mass of M_2 is significantly lower than the primary mass, the timing properties of QPE and the initial temperature of the cloud are set just by disk properties.

It is important to know that QPEs could be induced by impacts between BHs or very massive stars. To avoid complicated reasonings about the star structure and its change through the impacts we will focus solely on the BH case.

Statistics of QPEs

Right now we are ready to jump into simple data processing to infer some conclusions (or discussions) regarding this 5-year old phenomenon. In Fig. 4.1 physical properties are put that are crucial and different for each source. We should also present SMBH mass uncertainties because the black hole mass is not determined from the QPE data but mainly from empirical correlation of stellar velocity dispersion (in a galaxy bulge) to the central black hole mass (Gültekin et al., 2009). After determining the intervals of right values of BH masses we find that all values basically lie in the interval of $10^{x\pm0.5}\,M_{\odot}$. Therefore we do not show the uncertainties graphically.

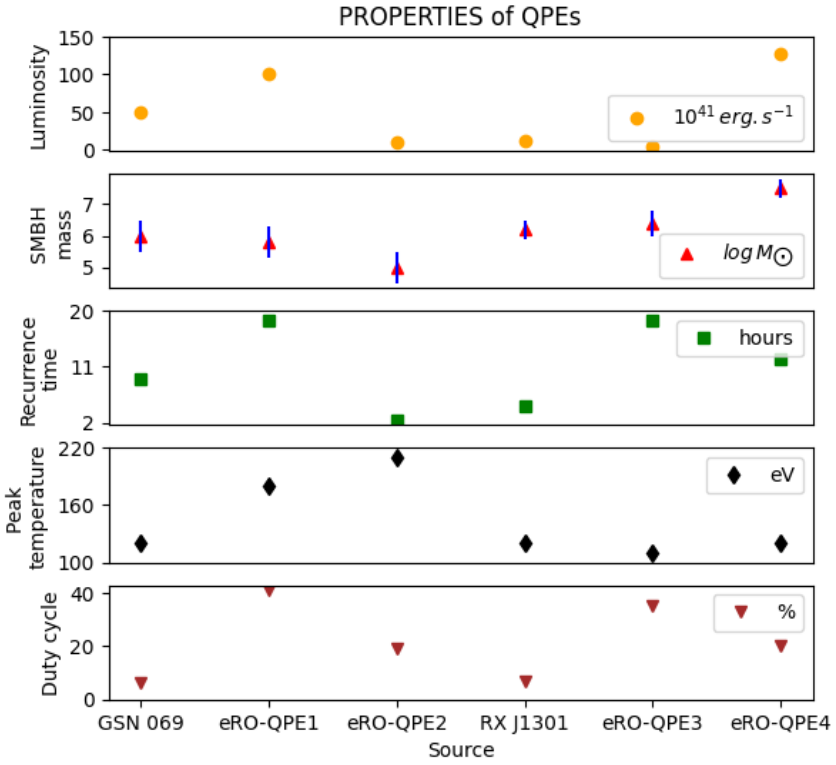

Figure 4.1: Plotted properties of different QPE sources (Swift J0230+28 excluded). Luminosity value is the average peak luminosity of light curves from one continuous measurement. Recurrence time is the time length between two consecutive bursts (data are taken straight from the articles cited in the section 2).

We did not include Swift J0230+28 because its recurrence time greatly exceeds the limits of the middle graph (it is on the order of days not hours). Nevertheless we made another visualization of QPE properties (with the Swift source) but with four subplots instead of five to give justice to all relevant data (Fig. 4.2).

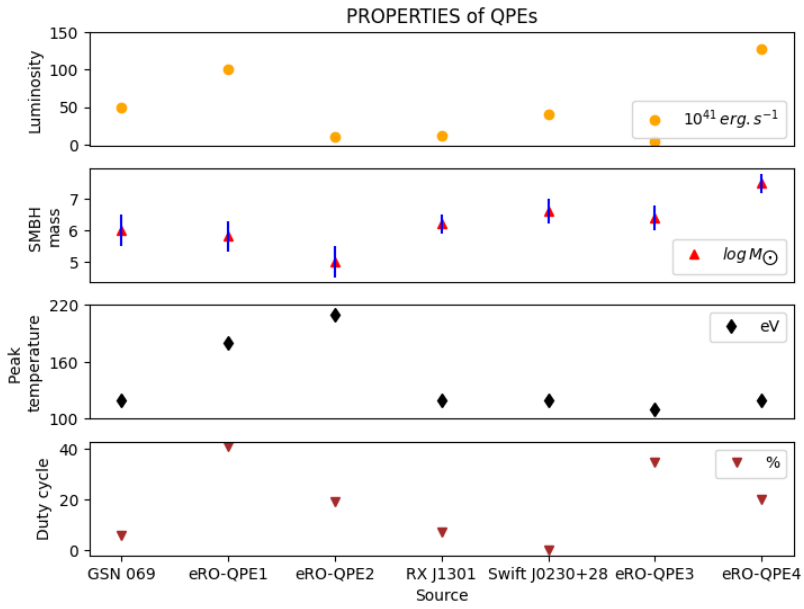

Figure 4.2: Plotted properties of different QPE sources (Swift J0230+28 included.)

To better see the variability across different QPE sources we show the reader two light curves from the longest continuous observations given for each source: *XMM4* and *Swift/XRT* observation of GSN 069 and Swift J0230+28 (Fig. 4.3).

4.1 Period Determination

There are lots of ways for determining the period of a source that behaves periodically. It all comes down to the light curves that we want to work on. If we are lucky enough to have so many data points that we can see all the phases (in one cycle) and the points are close, it is easy to just measure the distance between extremes (maxima or minima). The extreme can be found out by fitting a polynomial in the vicinity of it, polynomial extreme is then given to us by its formula. We will do it for each extreme in our data set of light curves and work out the average. The source is periodic if the standard deviation of periods we measured is is small compared to the average periodicity we take as a result. Relatively big standard deviation means that the astronomical source of light curves is not strictly periodic but quasi-periodic.

However, we do not have many data points within the rise or the decay of the eruptions. We have to employ a more sophisticated algorithm. We choose three methods of determining the periodicity of the source: Fast Fourier Transform (FFT), Lomb-Scargle

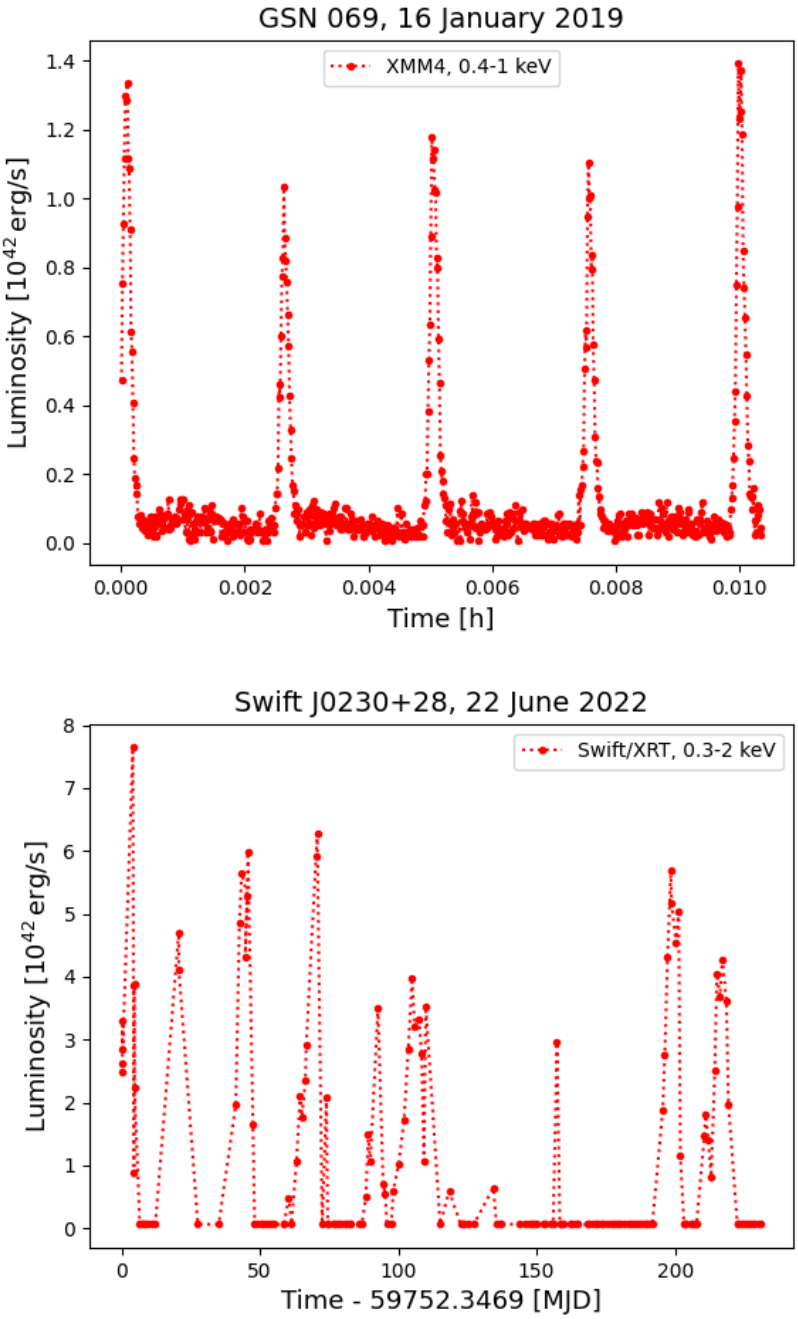

Figure 4.3: Different timescales and flare shapes across quasi-periodic eruptions.

Algorithm (LS) and The Wavelet Transform (WWZ). We determine the periodicity of each source with all three methods.

4.1.1 GSN 069

Because of the effect called ”aliasing” (explained later) we have multiple peaks derived from the biggest one. They do not carry any information on their own. The inferred periods are **9.3 h** from FFT and Lomb-Scargle periodograms and **9.1 h** from WWZ. The periodograms are in Fig. 4.4

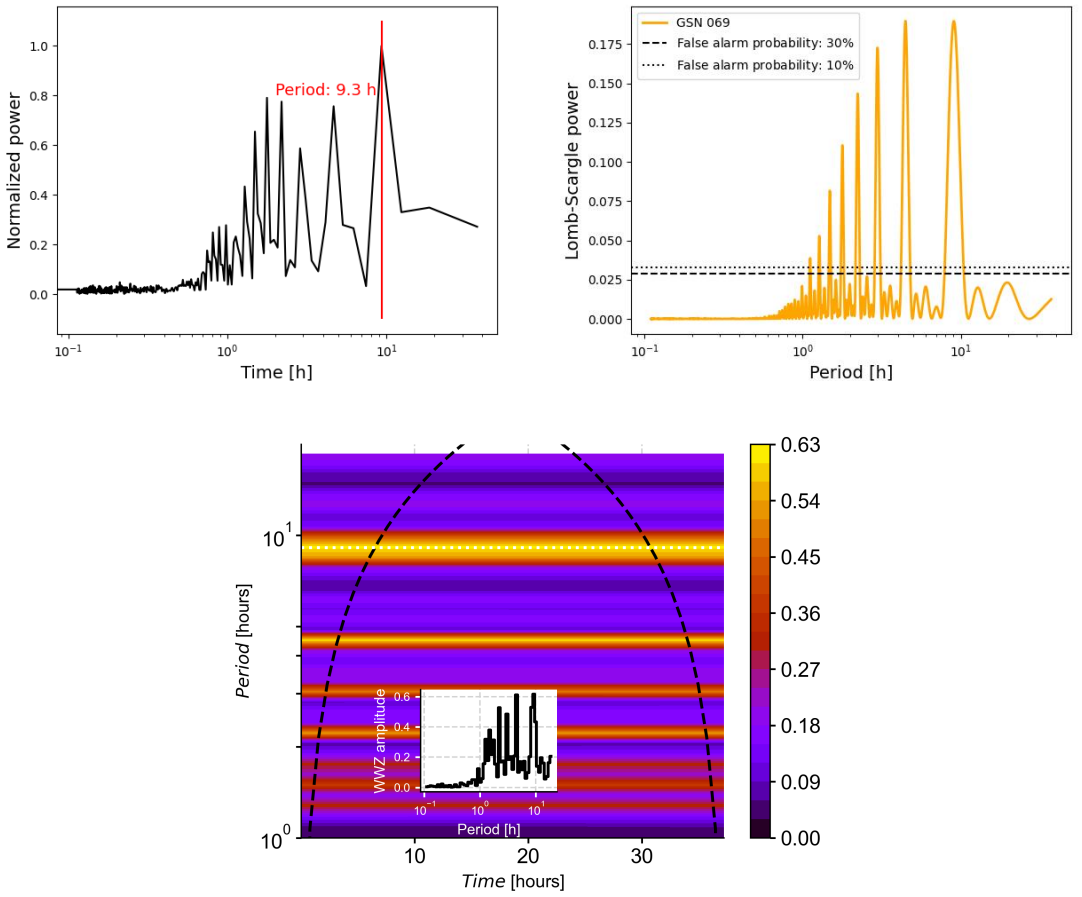

Figure 4.4: Period analysis of GSN 069. Upper left: FFT, **Uper right:** Lomb-Scargle, **Bottom:** WWZ.

4.1.2 eRO-QPE1

As we analyzed our first source, FFT offered indisputable solution. Normalized power shows a clear peak at **20.8 hours** (red color) while other peaks are half the size at most (Fig. 4.5).

However the situation is completely different with Lomb-Scargle algorithm where our supposedly correct answer for period length lies elsewhere (**18.2 hours**) and the corre-

sponding peak is not even the highest. This position belongs to x-coordinate 1.43 hours. Although we got a wrong answer, after analyzing the data set we found out that within data points in quiescence level consecutive points show spacing almost always 1.4 hours.

Finally, the WWZ transform shows a clear color distinction at **19.6 h** (white dotted line on 19.8 hours) with the second strongest pink region goes through 10 hours mark. This will be explained later as the ratio of these two highest values comes out almost exactly as two.

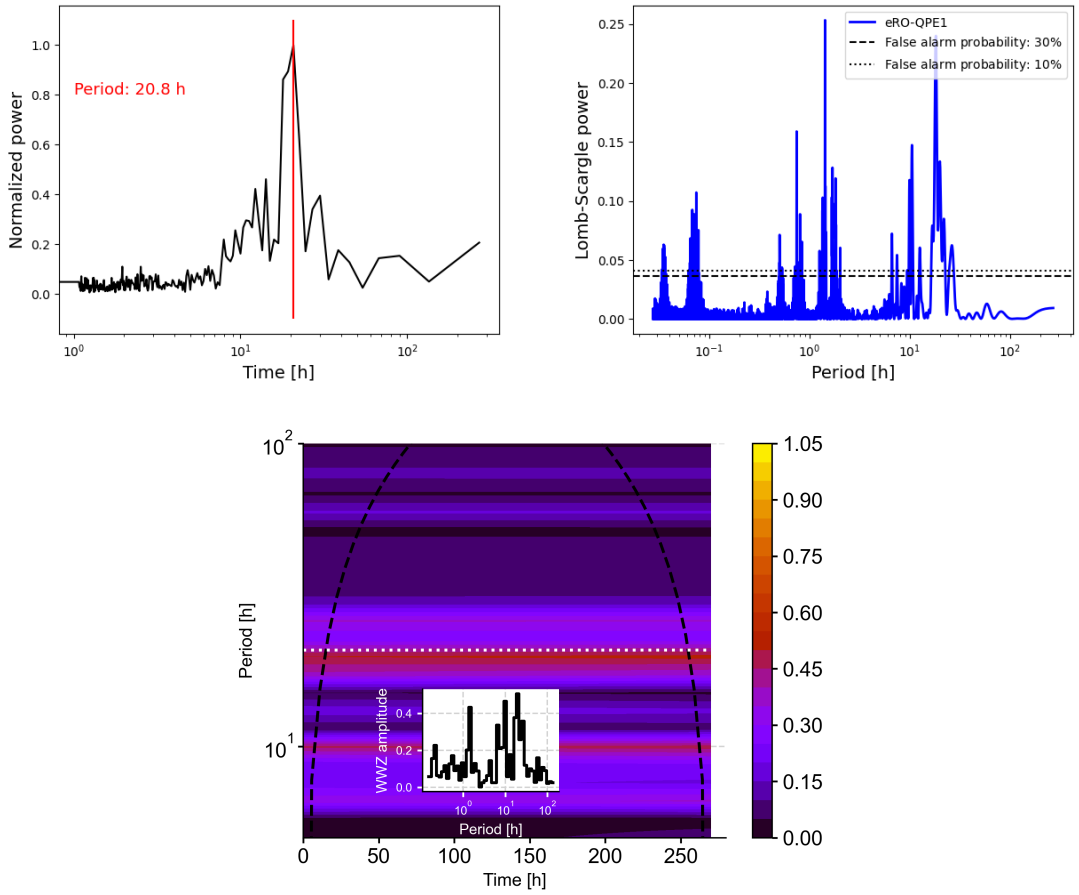

Figure 4.5: Period analysis of eRO-QPE1.

X-ray observation of eRO-QPE2 we have gotten has one particular quirk we noticed. Time spacing between all data points is exactly the same: ≈ 0.041 hours. All periodograms 'suffer' from this by creating peaks as a whole–number multiples of the biggest peak at frequency **2.4–2.5 h** (Fig. 4.6). Highest powers on the vertical y-axis are in order: 2.4, 1.2, 0.6 hours and so on. All periodograms show basically the same thing.

As for our most variable source, Swift J0230+28, period determination looks easy as the FFT and Lomb-Scargle periodograms share the same conclusion for **25.7 d** (4.7). But if we look at the wwz transform and analyze the 2D cross-section at the bottom, the highest amplitude is not so high as compared to other peaks (color map is not with clear

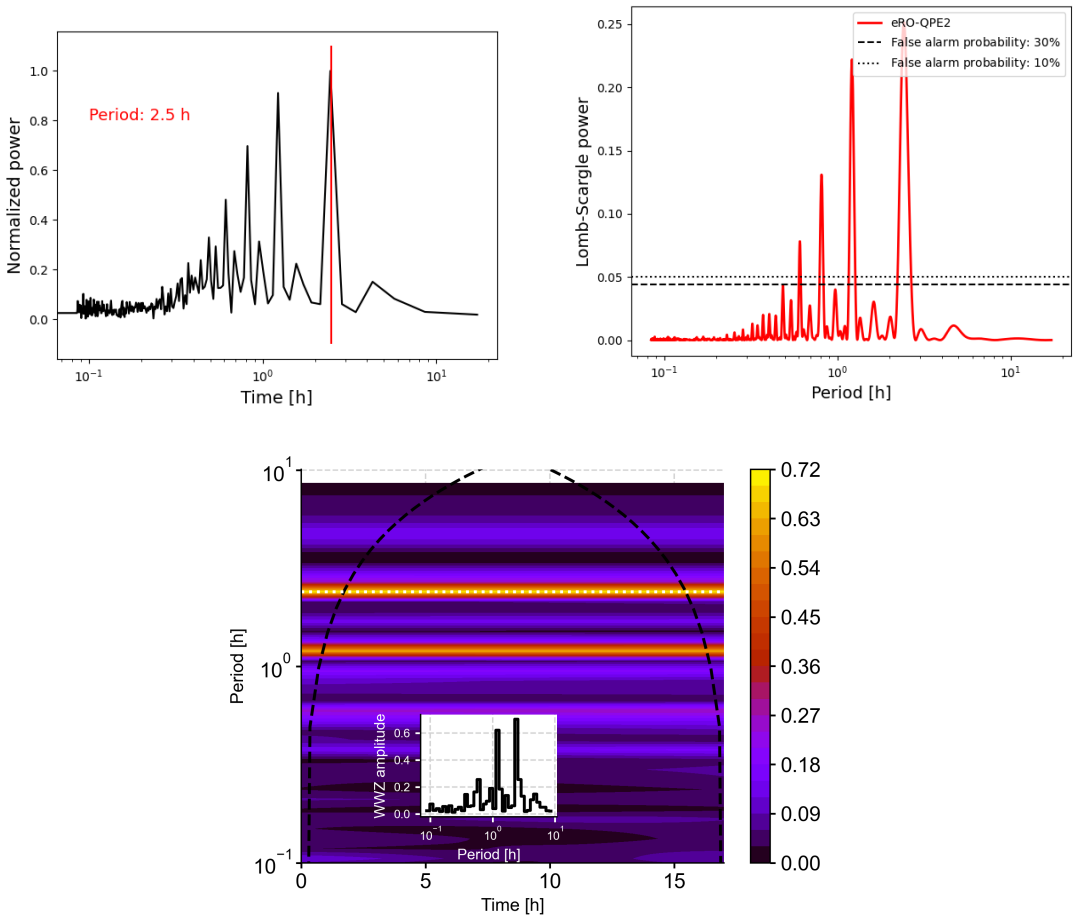

Figure 4.6: Period analysis of eRO-QPE2.

horizontal orange cuts as before). In other words, this periodogram comes with significant uncertainties.

The data for measured light curves eRO-QPE2 and GSN 069 are evenly spaced. That caused an effect called "aliasing" where the period is determined by one peak and followed by subsequently smaller peaks in time positions smaller by a whole number. This is most clear in Lomb-Scargle periodograms. The first peak from the right is followed by other at half of the x-value, other one at one quarter of the x-value, and so on.

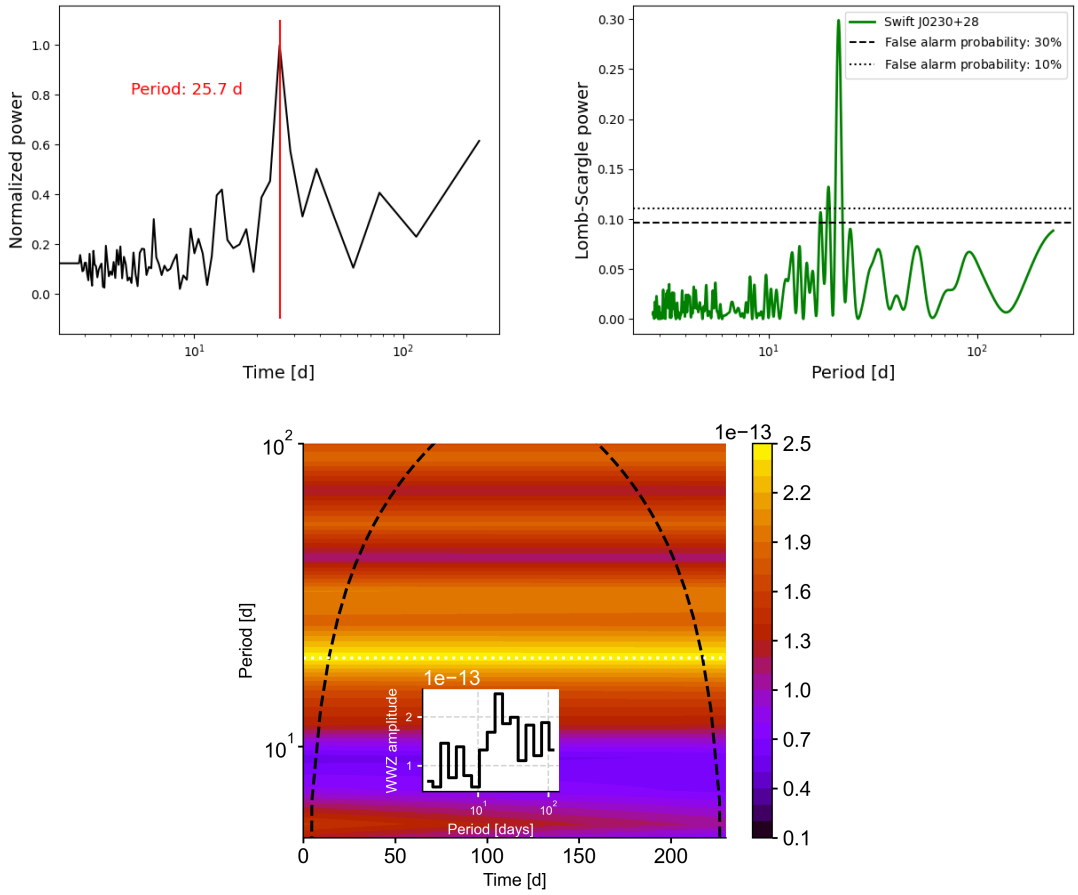

Figure 4.7: Period analysis of Swift J0230+28.

4.1.3 QPE Asymmetry

To better understand possible mechanisms behind individual QPE sources, we can analyze the symmetry of the peaks. The crude way to do it would be to fit a Gaussian curve to each eruption. Gaussian is by definition a symmetric function and the eruptions are mostly asymmetric meaning that the rise in luminosity is faster than decay (or the other way around). Therefore we can imagine an asymmetric Gaussian curve fitted to the eruption that is not symmetric to its center (has "different sigma" on the left side than the right). We can measure the time distance from the peak to the quiescence level on the left and

then right and infer the ratio. Main disadvantage of this approach is determining where the quiescence level begins.

The second, better method would be to fit the "Gaussian" itself to a whole eruption. We adopt an approach from (Barlow, 2004) documented in the *Form 5: Variable Gaussian*. Source code we used is pasted in the 5.3. As an example we show the fit of the last eruption in the GSN 069 source (Fig. 4.8).

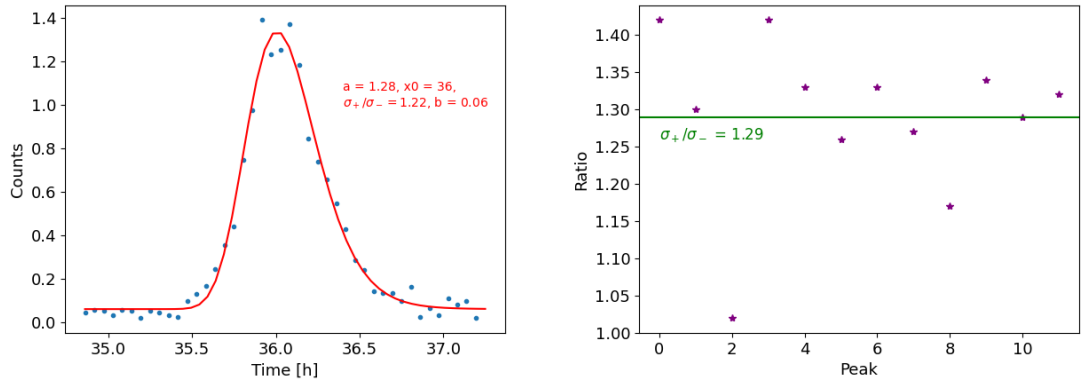

Figure 4.8: Top: Gaussian fit of the last eruption (GSN 069, 16 January 2019). Parameters of the fit are: a – amplitude, $x0$ – mean value, σ_+/σ_- – ratio, b – quiescent level in counts. **Bottom: Asymmetry of the eRO-QPE1** (19 August 2020). Average value is shown in green.

From the data we have processed (except Swift J0230+28 light curves that are nearly impossible to analyze this way) we found out that all eRO-QPE1, eRO-QPE2 and GSN 069 are asymmetric with the σ_+/σ_- ratio of more than 1 for all. In the Fig. 4.8 we show results from eRO-QPE1 analysis. From the other two, ratios are 1.25 and 1.12, respectively.
In the article (Franchini, Alessia et al., 2023), their artificial light curves have instantaneous rise and Gaussian decay. The sigma ratio would then be theoretically infinity. If the EMRI model from Franchini et. al. is in principle correct there must be additional effects changing the look of QPE light curves. We could consider simple reprocessing effect that can partially explain the ratio we have gotten. It would include effects of the environment onto the light-emitting cloud that changes the luminosity in different phases of the eruption and should prolong the rise of the eruption. On the other hand, the fact that rise is faster than decay could be a sign that we are on a right track since the same behaviour is modelled artificially. We refer the reprocessing of the light curves to a future work.

4.2 Time variability

Following the equation 1.10 we can verify if these quasi-periodic eruptions are just a result of an AGN variability timescale. The equation tells us that for accreting galactic nuclei this variability timescale is connected to standard timescales of the disk. If we express the right hand side ratio as a one quantity $X = \frac{M_\bullet^2}{\dot{M}}$ we can say that with growing T_B the X

grows as well. We plotted these the quantities from QPE sources and the result is in Fig. 4.9. For calculating $\dot{M}$ we used a formula 1.4 with $\eta = 0.1$.

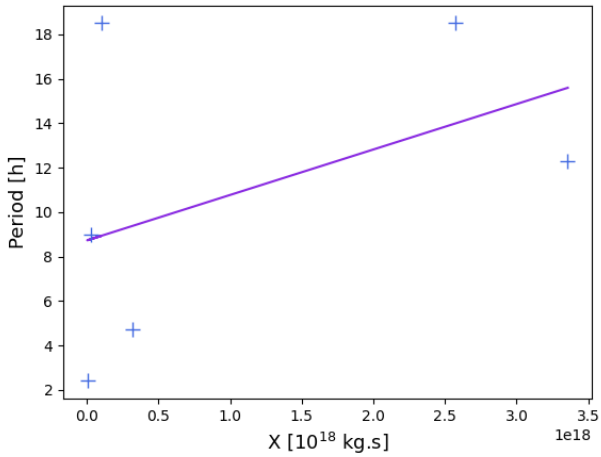

Figure 4.9: Variability timescale. Slope of the fit: $2 \pm 2 \cdot 10^{-18}\,\mathrm{h.kg^{-1}.s^{-1}}$

As we can see, the correlation is not significant because our fit has large uncertainties. With better mass determination of the MBH and the accretion rate this could give us a good approximation if QPEs are result of accretion disk instabilities.

4.3 Correlations of Different Properties

In this section we will discuss important physical properties that are possibly linked together and explain their connection. To do this we need to use a tool that will determine that connection.

4.3.1 Correlation Coefficients

Possibly two most popular procedures that determine variable connections are Pearson and Spearman corelation. Both of these describe common trend for two variables and how strong the trend is, as well with the value that describes how reliable the result of the correlation is. There are also differences with the two strongest ones being:

1. type of trend the variables comply (or not)

2. sensitivity concerning the individual points

Pearson's coefficient is used to describe linearity between two variables. Its value as a symbol r is determined by equation:

$$r = \frac{\Sigma\,(x_\mathrm{i} - \bar{x})(y_\mathrm{i} - \bar{y})}{\sqrt{\Sigma\,(x_\mathrm{i} - \bar{x})^2\,\Sigma\,(y_\mathrm{i} - \bar{y})^2}}, \tag{4.29}$$

where x_i is the variable x in the data and $\bar{x}$ is her arithmetic mean (similarly for y variable). That computes a value from interval $[-1,1]$. Exact value of -1 is for the exact linear decrease, 1 is for the exact linear increase. Value of 0 means there is no correlation between data sets.

Spearman's coefficient can be also used to describe linearity but is more general since it can describe correlated variables that do not have to follow linear trend but monotonic trend (i.e. also power law, exponential decay and so on). It is calculated accordingly:

$$\rho = 1 - \frac{6\Sigma d_i^2}{n(n^2-1)}, \tag{4.30}$$

where d_i are differences between the two ranks in each observation and n is the number of observation. This coefficient returns the same interval of values.

For determining the correlation we need both coefficients. Here is why.

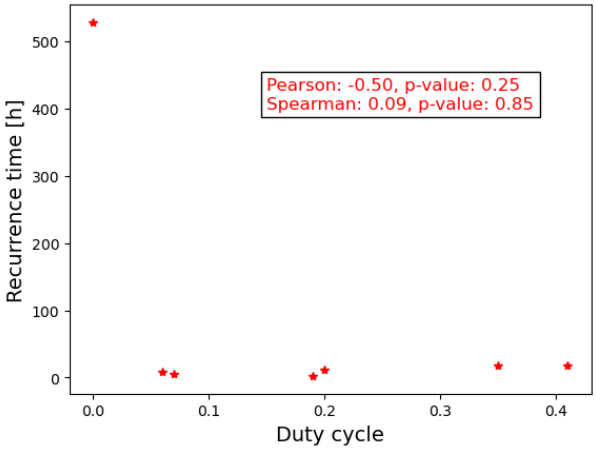

Figure 4.10: Difference between coefficients.

In the Fig. 4.10 we have calculated both coefficients from our data. It shows connection between QPE duty cycles and recurrence times. Visually there is an outlier (extreme period of Swift J0230+28) that makes impossible to determine the connection. However the coefficients show very different values. 'Pearson' shows different value than 'Spearman'. Despite clear correlation (that is proven later) between six points, our outlier ruins the result. This points to the conclusion that Pearson coefficient is very sensitive to extremes in the data. After removing the outlier, coefficients yield very similar result.

After analyzing QPEs we found out two important correlations (Fig. 4.11). First one is a correlation of central SMBH mass and peak temperature (highest temperature of the disk during the flares). It could imply that with smaller central black hole the peak temperature of the flares gets higher. This inverse proportionality can be generally explained from temperature dependence on distance from the black hole, its mass and accretion rate:

$$T = \left(\frac{3GM_\bullet \dot{M}}{8\pi R^3 \sigma}\right)^{1/4}, \tag{4.31}$$

where σ is the Stefan-Boltzmann constant. If we express R in terms of R_{ISCO}, the main scaling parameter of the system, we get proportionality

$$T \propto M^{-1/2}, \tag{4.32}$$

that could theoretically explain this correlation. It can be also explained with our EMRI system model: for a fixed period of the smaller companion, the higher the SMBH mass the orbit of EMRI is further so it also crashes with accretion disk in places further from the centre. But with increasing radial distance the temperature decreases as can be seen from 4.31.

From the Recurrence time – Duty cycle correlation it seems that with increased time intervals between the flares the duration of the flares increased as well. This can be hardly explained without relying on a particular model. We have to note that the significance of the correlation coefficient determination is given by p-value. That is a number defined as a probability that we would find the same result if the correlation was zero. Statisticians like if the p-value is below 0.05 (5%). In our case that is only true for Pearson c. in the first graph. These coefficients are only orientational since we do not have many data points and the resulting correlation is only orientational.

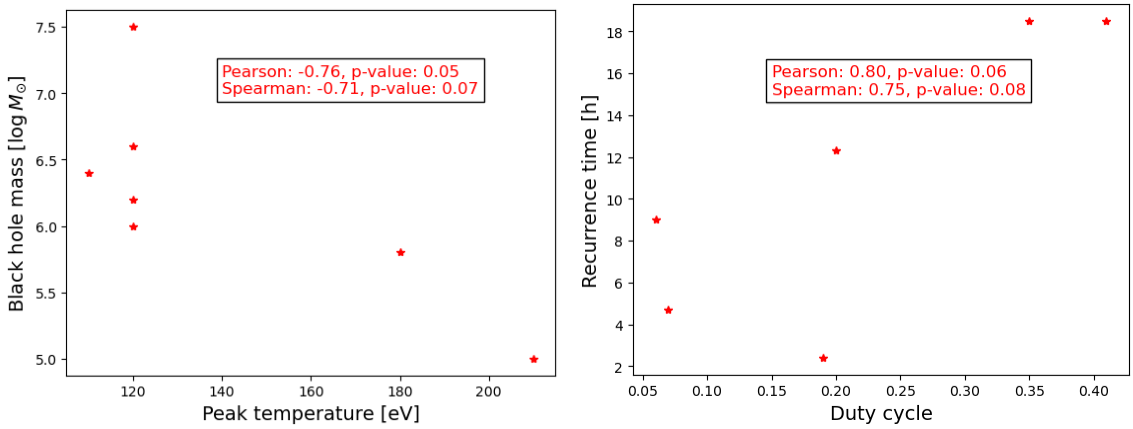

Figure 4.11: Correlation coefficients within the graphs. The graph on the right does not include Swift J0230+28 (again because of its large recurrence time).

4.4 Long-term Evolution

In an article (Pasham et al., 2024) new observations of eRO-QPE1 are reported from multiple epochs throughout years 2021–2023. Light curves are shown in Fig. 4.12. As we go through the epochs the decrease is evident as the scale of y-axis changes.

We can use the data points from all these epochs: calculate the long-term decrease of count rates. We did exactly that (except for data from epoch #4 and #6) and for the period as well. We picked count rates with assigned times and plotted the result along with linear fit of the data. Results are in the Fig. 4.13.

From the count rate decrease we can estimate (very crudely) the lifetime of the QPE system as we could extrapolate from these light curves. As we can see the y-axis intercept is fitted at 0.05 counts while after 600 days mark the y-value is halved. From the last

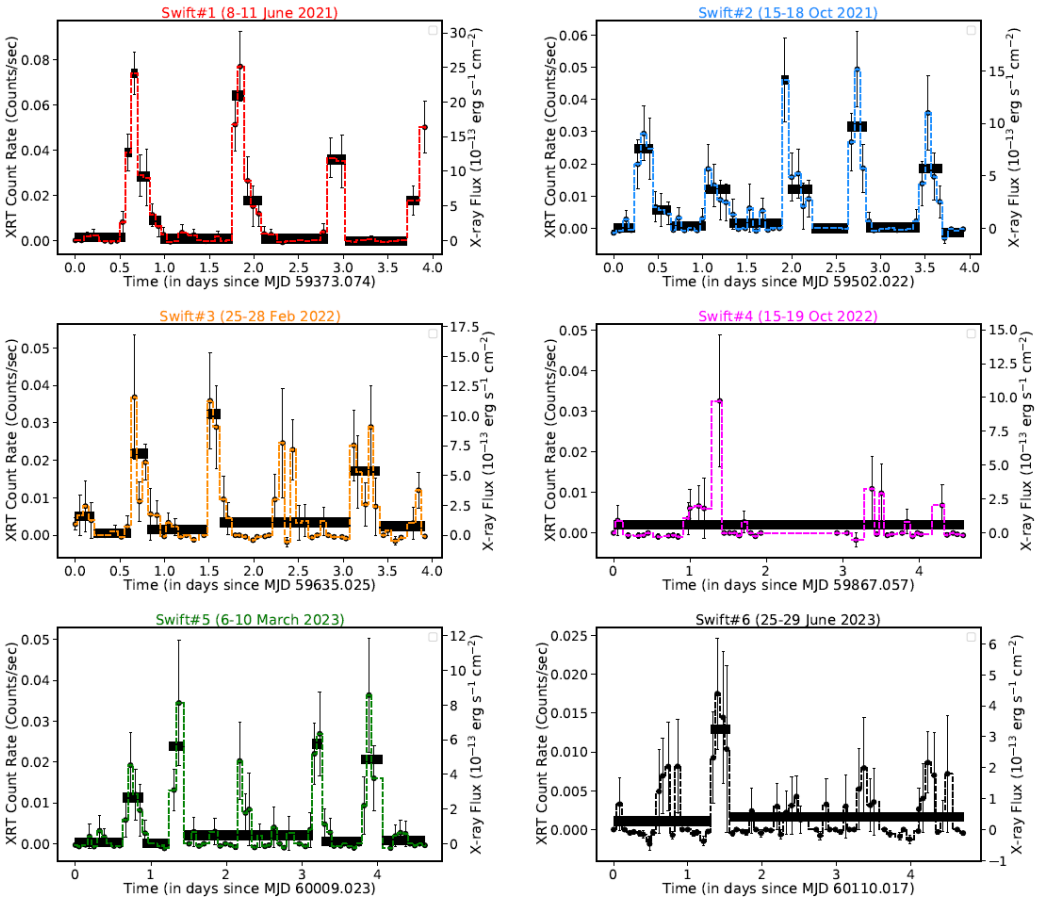

Figure 4.12: 0.3–1.2 keV X-ray light curves. Each light curve is from a monitoring program Swift. The thick black horizontal lines are the optimal time bins.

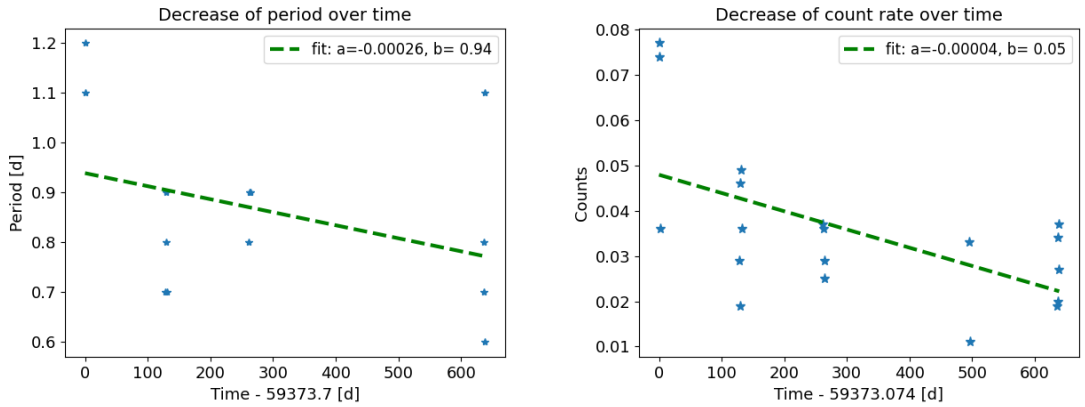

Figure 4.13: Period and count rate decrease of eRO-QPE1 in the horizon of two years. Data points are fitted with a line $a \cdot x + b$. Unsurenesses of the period fit are: $\sigma(a) = 0.002, \sigma(b) = 0.08\,d$. With count rate fit: $\sigma(a) = 0.00001\,d^{-1}, \sigma(b) = 0.01$.

epoch in Fig. 4.12 we can estimate the count rate by which it is almost impossible to detect individual eruption with peak. The critical count value estimated here would be somewhere between 0.005–0.01 (approximately ten times less the intercept of y-axis in 4.13). If the current tempo of losing energy in the eRO-QPE1 system will continue in the same linear fashion the eruptions will be no longer detectable in June 2025. We assumed the faintest count rate detection, that the trend will continue linearly and that the system will not gain energy through any other processes.

We can also predict the lifetime of eRO-QPE1 theoretically if we consider the system of a SMBH surrounded by accretion disk orbited by a small companion. The cloud luminosity resulting from a crash of an EMRI with the disk gets smaller with the size of the cloud itself. If we consider the properties of the EMRI orbit to change faster than the disk properties the observed luminosity decrease can be explained by shrinking of the R_{inf} (3.21) through faster v_{rel} that comes with smaller semi-major axis. In other words, the closer EMRI companion gets to the black hole the dimmer the eruptions will be.

Two main mechanisms could cause this effect: crashing with the disk slows down the companion and results in greater gravitational pull towards the center of the system. Through this mechanism the system is losing energy. Typical time for this to happen is called magnetohydrodynamical timescale and is investigated in the article (Narayan, 2000). Other mechanism through which the system can lose energy is emitting gravitational waves. This was also investigated quantitatively in the article (Peters, 1964) where merger timescale is introduced. After this time the system loses a certain amount of energy only through gravitational waves. We want to investigate only one dominant mechanism of an EMRI losing energy. In the article (Kejriwal et al., 2024) covering systems that could be potential candidates for LISA observations of gravitational waves, these two timescales are compared (Fig. 4.14). For parameters of all QPE systems that were discovered (yet) the shorter timescale is the hydrodynamical timescale.

From the Fig. 4.13 we see that the count rate dropped in 2 years by one half. From the Toy model (5.1) we can find out how long would it take for the peak luminosity of the flares to drop by one half. Since accretion disk loses its mass, we can manually lower the accretion rate $\dot{m}$ until the peak luminosity drops below one half. This will happen if $\dot{m}$ drops by a factor of ~ 35.

The luminosity of the eruption could also drop because of the gravitational waves that steal energy from the system. But it would have to be very close, on the order of a few gravitational radii.

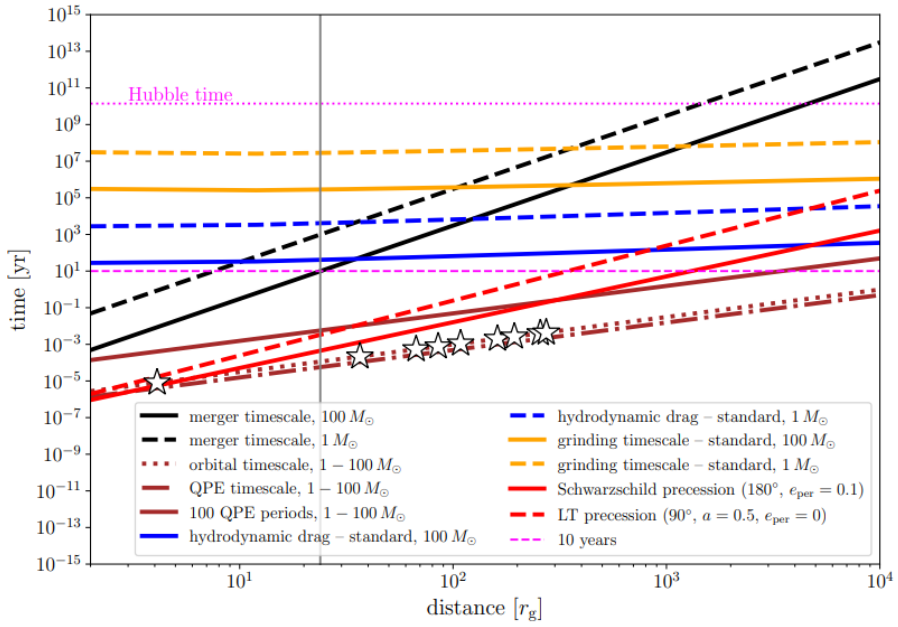

Figure 4.14: Different timescales for companions with different masses. Timescales in years dependent on the distance (in R_g) from the MBH with mass $10^6\,M_\odot$. Dynamical processes - grinding, hydrodynamical drag and merger are shown in the legend. Solid line corresponds to CO mass $100\,M_\odot$ while dashed lines correspond to CO mass $1\,M_\odot$. Vertical solid line at the distance of $\sim 24\,R_g$ corresponds to the orbital period of 1 hour. Timescales are estimated for the standard disk with relative accretion rate of $\dot{m} \sim 0.1$, initial inclination of the CO is 15°. The stars represent the positions of detected quasi-periodic sources. Credit: Kejriwal et al. (2024).

Results from Toy model and Long-term Evolution

5.1 Toy Model

In this thesis, we create artificial light curves according to the article (Franchini, Alessia et al., 2023). For our specific needs the model is substantially simplified - we neglect the effects from general relativity and all kinds of precessions. Basically, we focus on creating periodic light curves in terms of timing properties.

To be more specific, we list all the points that are going to be neglected in the Toy Model:

1. Gravitational wave emission
2. Precession of the disk around the MBH
3. Lense-Thirring precession of the disk
4. Apsidal and nodal precession of the EMRI companion

The trajectory of the EMRI companion is purely Keplerian, so the semi-major axis a, period P, and black hole masses M_1, M_2 are connected by the Second Kepler's law:

$$\frac{P^2}{a^3} = \frac{4\pi^2}{G(M_1 + M_2)}, \tag{5.33}$$

where we can neglect the mass of the companion M_2 since it is much smaller than M_1.

As a disk model we take the "standard model" of α-disk investigated by Shakura and Sunayev. The disk reaches into the R_{ISCO} depending on the spin of the MBH, χ. Its mass is distributed with a power-law surface density profile Σ, its average volume density on a given radius is ρ, its height H is the width of the disk at a given radius, and the temperature profile is T.

$$\Sigma = 5.2\,\alpha^{-4/5}\dot{M}_{16}^{7/10} m_1^{1/4} R_{10}^{-3/4} f^{14/5}\,\mathrm{g.cm^{-2}} \tag{5.34}$$

$$H = 1.7\cdot 10^{8}\,\alpha^{-1/10}\dot{M}_{16}^{3/20} m_1^{-3/8} R_{10}^{9/8} f^{3/5}\,\mathrm{cm} \tag{5.35}$$

$$\rho = 3.1\cdot 10^{-8}\alpha^{-7/10}\dot{M}_{16}^{11/20} m_1^{5/8} R_{10}^{-15/8} f^{11/5}\,\mathrm{g.cm^{-3}} \tag{5.36}$$

$$T = 1.4\cdot 10^{4}\alpha^{-1/5}\dot{M}_{16}^{3/10} m_1^{1/4} R_{10}^{-3/4} f^{6/5}\,\mathrm{K} \tag{5.37}$$

$$\text{with } f = \left[1-\left(\frac{R_*}{R}\right)^{1/2}\right]^{1/4}. \tag{5.38}$$

where α is the Shakura-Sunayev viscosity parameter, $\dot{M}_{16}$ is the accretion rate of the MBH in $10^{16}\,\mathrm{g.s^{-1}}$, R_{10} is the radius scaled to $10^{10}\,\mathrm{cm}$, m_1 is the mass of the central black hole (equations are taken from Frank et al. (2002)). The R_* in the parameter f is for us the innermost stable circular orbit. There are more equations in the Shakura-Sunayev model telling us informations about other properties, such as radial drift velocity, opacity, and more. We need only those that are in 5.34–5.38. The material in the accretion disk moves around the MBH with Keplerian velocity mentioned in the section 3.1.2. We infer the accretion rate of the MBH from the quiescent bolometric luminosity of the source from the equation 1.4. We choose the efficiency of the accretion as 10% for slowly rotating black hole while for bigger black hole spin we increase the efficiency.

The companion crosses the disk always twice per orbit with relative velocity towards the material of the disk. We then calculate the emission in the same way shown in the section 3.1.4.

5.2 Artificial curves

In this section we fit light curves of GSN 069, eRO-QPE1 and eRO-QPE2 with the Toy model. Firstly, we fit the light curves with the same parameters as in (Franchini, Alessia et al., 2023). But we have never gotten the same profile. There are many ways how can we change the parameters so that the light curves sit well on data but we choose to modify the parameter M_2, mass of the companion. This mass parameter has the same value for all artificial curves in the original article. They always consider $M_2 = 100\,\mathrm{M_\odot}$. The quiescent level of synthetic light curves is made to be the same as in the measured data.

In the Fig. 5.1 we created light curves for GSN 069 with following parameters: quiescent bolometric luminosity is $3.5\cdot 10^{43}\,\mathrm{erg.s^{-1}}$, black hole rotates slowly with a spin $\chi = 0.1$, the accretion efficiency is $\eta = 0.1$, the secondary orbits on a slightly eccentric orbit with $e = 0.1$ with inclination i = 10° with orbital period $P = 18\,\mathrm{h}$ and semi-major axis $a = 160\,\mathrm{R_g}$. The mass of the black hole is $10^6\,\mathrm{M_\odot}$.

To get the desired profiles we change the M_2 to 70 $\mathrm{M_\odot}$ and excentricity to 0.01. Our model nicely produces desired peak luminosities and timing properties.

We then try to replicate eRO-QPE2 data with parameters: quiescent bolometric luminosity is $5.5\cdot 10^{41}\,\mathrm{erg.s^{-1}}$, black hole rotates with a spin of $\chi = 0.5$, we choose the accretion efficiency $\eta = 0.2$, the secondary orbits on almost circular orbit with $e = 0.05$

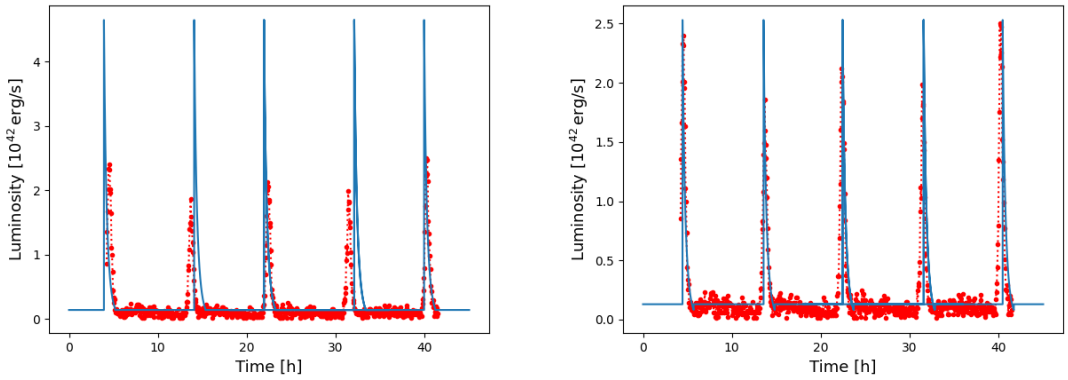

Figure 5.1:
Left: GSN 069 fitted with parameters from (Franchini, Alessia et al., 2023).
Right: Toy model fits the data better with circular orbital trajectory.

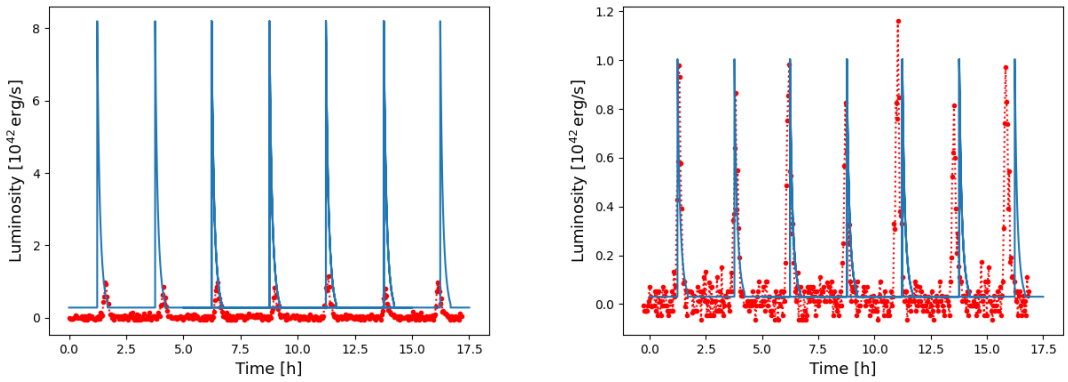

Figure 5.2: Left: Original fit of eRO-QPE2. **Right:** Toy model.

with inclination $i = 15\%$ with orbital period $P = 5\,\mathrm{h}$ and semi-major axis $a = 320\,\mathrm{R_g}$. Black hole in this case is less massive with $M_1 = 10^5\,\mathrm{M_\odot}$.

To get the desired profiles we change the M_2 to 35 $\mathrm{M_\odot}$. The profiles fit well on top of each other but we can see a small deviation in the 5th peak at the end. The resulting fit is in Fig. 5.2.

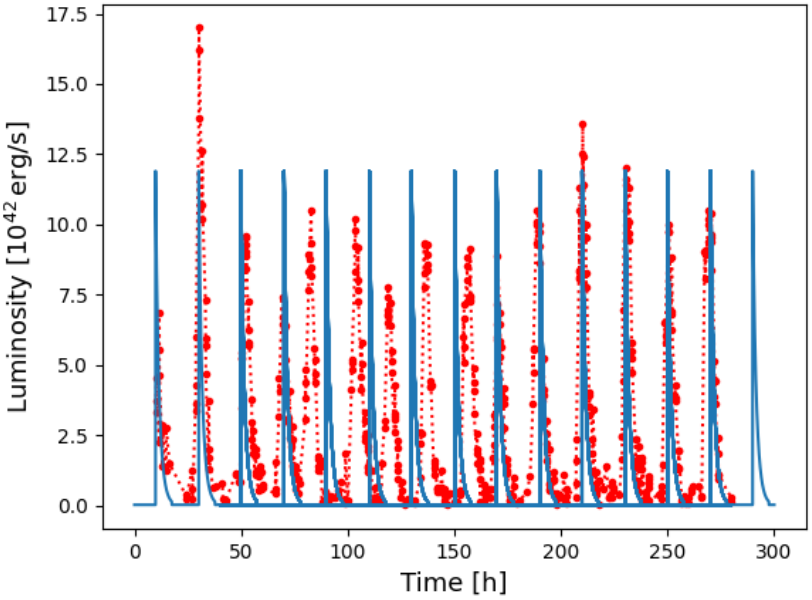

Figure 5.3: Toy model tested for eRO-QPE1.

In this source the quiescent level was not detected but it is estimated to be below $\sim 1.6 \cdot 10^{41}\,\mathrm{erg.s^{-1}}$. The black hole mass is $10^{5.8}\,\mathrm{M_\odot}$ and spins faster with $\chi = 0.65$. The secondary orbital period is 40 h with semi-major axis of 355 $\mathrm{R_g}$, the eccentricity is $e = 0.05$ and inclination i = 20°. The black hole efficiency is chosen to be $\eta = 0.3$.

Here the luminosities are extremely low, even under $10^{41}\,\mathrm{erg.s^{-1}}$ and we do not show the resulting fit. To get into measured orders of magnitude we had to increase the secondary mass up into $M_2 = 600\,\mathrm{M_\odot}$. This source alternates its period as we can see from the middle of the Fig. 5.3. The desired luminosities can not be produced individually with the Toy model so we produced only average peak luminosity.

5.3 Parameter Variations

In this small segment we show how a variation of a different parameters impacts the light curve properties. All results are in the Fig. 5.4 where dotted line is an artificial light curve from 5.1 with $M_2 = 100\,\mathrm{M_\odot}$. We change excentricity to $e = 0.5$, the BH spin from 0 to 1, the inclination down to very small values where the plane of the disk is almost coincident with that of the orbit of the companion. Finally, we show the variation of the Shakura-Sunayev α parameter from 0.01 to 0.3. As we can see, the BH spin has a relatively small impact compared to other parameters being changed. For example, with

coincident planes of the CO orbit and the accretion disk, the relative velocity between the CO and material in the disk is almost zero, so the sphere of influence diverges to infinity (see equation 3.21).

To better see all 3 colors in one graph we shifted the light curves from each other by one hour each, otherwise the strongest would cover those behind.

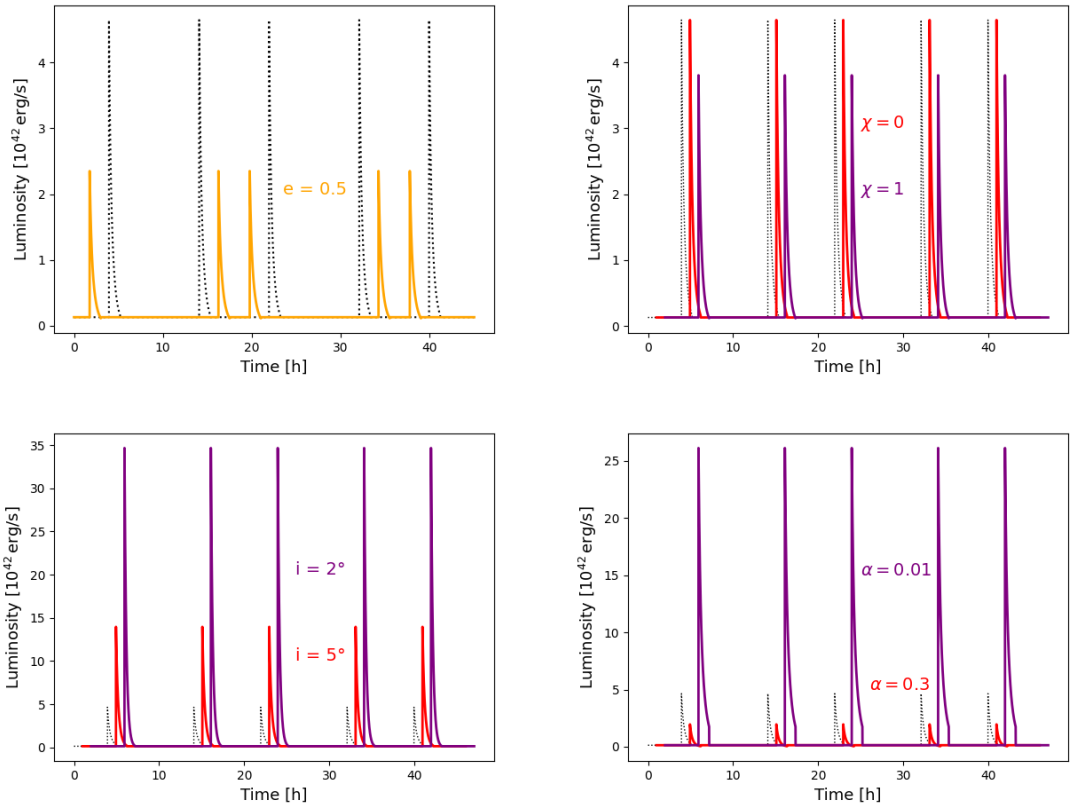

Figure 5.4: Impact of different parameters on the timing properties and amplitudes. **Top left:** Excentricity. **Top right:** BH Spin. **Bottom left:** Inclination. **Bottom right:** Viscosity parameter.

Conclusion

Our aim was to statistically process the data at hand and come up with quantitative results about the QPE properties. Concerning the timing properties we calculated the periods for 4 sources and got definitive results for their values. They agree with values determined in the articles of their observations. Then we performed an analysis on the shapes of the eruption profiles, with help of the asymmetric Gaussian fit. In all cases, the decay/rise ratio was bigger than one, implying that different QPE sources could have the same physical origin. The source Swift J0230+28 is still an extremely difficult task for both of these methods of analyzing timing properties. The problem is not so much in the periodicity but in the lack of data points and not knowing its quiescent level.

With use of the correlation coefficients we determined the connection between different QPE properties such as the central black hole mass, recurrence times, and so on. We have found out two correlations, one of which proves that the EMRI model could be the right one (correlation between MBH mass and peak temperature of the eruptions) and the other one disproves it. There were no other significant correlations. After the new phase of eRO-QPE1 we predicted with a very simple idea that the source will stop sending detectable signal in a few years. Lifetime of a QPE source would be in years, then.

In another section we derived a simplified model for an EMRI system that creates periodic light curves and fitted it to 3 QPE sources. There was a good agreement between artificial light curves and measured data for eRO-QPE1 and GSN 069. To be more precise with the eruption profile we would need a better model that does not have an instantaneous rise. Finally, we described an impact of 4 physical parameters on the light curves. We have found out that the excentricity not only affects the timing properties but also values of luminosity peaks. A spin of the black hole has only a small impact. We also investigated how an inclination of the companion's orbit changes the amplitude for small values. Finally, the α-parameter was modified and the model diverges for extreme values.

This new class of X-ray AGN variabilities is difficult to analyze robustly because we do not have enough QPE sources to investigate. We only went through the most basic physical properties and some of them are far from definite conclusions. QPEs do not even have to be unified under a single physical model, each source can have a different driving mechanism. However, this work could serve as a guide to anyone who wants to start learning about this phenomenon since it covers the most basic facts. It is also an encouragement for anyone trying to describe these eruptions with an EMRI model since even our very simple Toy model is able to reproduce the main light curve properties, such as recurrence time, duty cycle, or amplitude. However, we can not reproduce the exact modulations in recurrence time and flare shapes. For that, a more sophisticated model is required and we defer that to the future work.

Appendix

Periodograms

Values of time series are marked by x. With discrete data we use the notation x_k, $k \in \{1,....,N\}$, measured at time t_k, and Δx_k shows the measurement uncertainties. We use $x(t)$ or x_t for simplicity ($t \in \mathbb{R}$).

Fast Fourier Transform

The formula for the discrete Fourier transform (DFT) of the set $\{x_\mathrm{k}\}_{\mathrm{k}=1}^{\mathrm{N}}$ is

$$DFT(f_\mathrm{s}) = \sum_{\mathrm{k}=1}^{\mathrm{N}} x_\mathrm{k} exp(-2\pi i f_\mathrm{s} t_\mathrm{k}) \tag{6.39}$$

for a set of frequencies $f_\mathrm{S} = \frac{s-1}{N\delta t}$, $s \in \{1,....,N\}$, where $\delta t = t_{\mathrm{k}+1} - t_\mathrm{k}$ is a time interval between following observations. The inverse of the interval is the sampling rate, $SR = = 1/\delta t$. The first point, $DFT(0) = \sum_{\mathrm{k}=1}^{N} x_\mathrm{k}$, is the zero-frequency value. If we subtract from the time series its mean we remove the DC value (first point) from the DFT. The Nyquist frequency is given by $f_\mathrm{Nyq} = 1/(2\delta t)$ and denotes the maximal frequency that can be inferred from the observed time series.

The Fourier PSD is then defined by

$$P(f_\mathrm{s}) = \frac{2\delta t}{N} |DFT(f_\mathrm{s})|^2. \tag{6.40}$$

The Poison noise level that comes from the statistical noise due to uncertainties in the measurements, Δx_k, is given by

$$P_\mathrm{Poisson} = \frac{2\delta t}{N} \sum_{\mathrm{k}=1}^{\mathrm{N}} \Delta x_\mathrm{k}^2. \tag{6.41}$$

For fitting the power-law in log–log space,

$$P(f) = \frac{P_{norm}}{f^\beta}, \tag{6.42}$$

or PL plus Poisson noise (PLC) power spectrum

$$P(f) = \frac{P_{norm}}{f^\beta} + C, \tag{6.43}$$

where P_{norm} is a normalizing constant and C is an estimate of $P_{Poisson}$. But in this case, evenly spaced frequencies f_s are not uniformly spaced anymore, when logarithmized. Solution for this is binning. Values of $\log f_s$ are binned into equal-width bins, with at least two points in a bin, and the frequencies are computed as a geometric mean in each bin. PSD value in a bin is the arithmetic mean of the logarithms of the PSD. Also, the logarithm of PSD is shifted upwards by $\gamma/\ln(10) \approx 0.250682$, so we get the correct bias-corrected PSD by subtracting this value from the logarithmic PSD.

Lomb-Scargle Periodogram

The LSP is a periodogram for unevenly samled time series. It is computed as follows:

$$P_{\mathrm{LS}}(\omega) = \frac{1}{2\sigma^2}\left(\frac{\left(\sum_{\mathrm{k}=1}^{\mathrm{N}}(x_{\mathrm{k}}-\tilde{x})\cos\left[\omega(t_{\mathrm{k}}-\tau)\right]\right)^2}{\sum_{\mathrm{k}=1}^{\mathrm{N}}\cos^2\left[\omega(t_{\mathrm{k}}-\tau)\right]} + \frac{\left(\sum_{\mathrm{k}=1}^{\mathrm{N}}(x_{\mathrm{k}}-\tilde{x})\sin\left[\omega(t_{\mathrm{k}}-\tau)\right]\right)^2}{\sum_{\mathrm{k}=1}^{\mathrm{N}}\sin^2\left[\omega(t_{\mathrm{k}}-\tau)\right]}\right), \tag{6.44}$$

where $\omega = 2\pi f$ is the angular frequency, $\tau \equiv \tau(\omega)$ is

$$\tau(\omega) = \frac{1}{2\omega}\arctan\left[\frac{\sum_{\mathrm{k}=1}^{\mathrm{N}}\sin 2\omega t_{\mathrm{k}}}{\sum_{\mathrm{k}=1}^{\mathrm{N}}\cos 2\omega t_{\mathrm{k}}}\right], \tag{6.45}$$

where $\tilde{x}$ and σ^2 are the sample mean and variance.

The lower limit for the sampled frequencies is $f_{\min} = 1/(t_{max} - t_{min})$. The upper limit is $f_{\max}$, also called the Nyquist frequency. This is the same frquency, as in the Fourier spectrum. In the case of nonuniform sampling, $f_{\mathrm{Nyq}} = 1/2p$, where p is the smallest value that satisfies the equation $t_{\mathrm{k}} = t_1 + n_{\mathrm{k}}p, n_{\mathrm{k}} \in \mathbb{N}$.

The frequency of the grid should not be too fine because that would require a long computational time. Also, it should not be too sparse, because it would miss structures between the grid points. It is considered a good choice to pick a grid so that each peak is sampled 5–10 times. The total number of sampling frequencies is then

$$N_{\mathrm{p}} = n_0\frac{f_{\max}}{f_{\min}}, \tag{6.46}$$

where we take $n_0 = 10$ after. Also, we need to adjust the Poisson noise level to the normalization used in the Equation 6.44:

$$P_{\mathrm{Poisson,LS}} = \frac{1}{2\sigma^2}\frac{1}{2\delta t}P_{\mathrm{Poisson}} \tag{6.47}$$

Wavelet scalogram

Wavelets

A wavelet $\psi(t)$ is a short, temporally and spectrally localized oscillation with finite energy and zero mean, $\langle\psi(t)\rangle = 0$. A mother wavelet generates the dictionary, or child wavelets, that form the basis:

$$\psi_{\mathrm{s,l}}(t) = \frac{1}{\sqrt{s}}\psi\left(\frac{t-l}{s}\right), \tag{6.48}$$

where $l \in \mathbb{R}$ refers to the location of the wavelet, and $s \in \mathbb{R}_+$ is the scale, corresponding to dilation. The prefactor is responsible for normalization across different timescales, $\langle \psi_{\mathrm{s,l}}(t), \psi_{\mathrm{s,l}}(t) \rangle = 1$. A CWT (continuous wavelet transform) enables the signal $x(t)$ to be decomposed into a combination of $\psi_{\mathrm{s,l}}(t)$ with the wavelet coefficients

$$W(s,l) = \langle x(t), \psi_{\mathrm{s,l}}(t) \rangle = \int_t x(t)\psi^*_{\mathrm{s,l}}(t)dt. \tag{6.49}$$

The signal can be reconstructed by:

$$x(t) = \sum_{\mathrm{s,l}} W(s,l)\psi_{\mathrm{s,l}}(t). \tag{6.50}$$

A discrete wavelet transform (DWT) is a CWT computed for a discrete set of translations and scales:

$$d_{\mathrm{j,k}} = \langle x(t), \psi_{\mathrm{j,k}}(t) \rangle = \int_t x(t)\psi_{\mathrm{j,k}}(t)dt, \tag{6.51}$$

with child wavelets

$$\psi_{\mathrm{j,k}}(t) = \frac{1}{2^{j/2}}\psi\left(\frac{t}{2^j} - k\right), \tag{6.52}$$

with $j \in \mathbb{Z}$ being the octave (timescale) and $k \in \mathbb{Z}$ the position of the wavelet. The octaves are divided into an integer number of voices.

For CWT the complex-valued Morelet wavelet is often used:

$$\frac{1}{\pi^{1/4}}\left[\exp\{i\omega t\} - \exp\left\{-\frac{\omega^2}{2}\right\}\right] \cdot \exp\left\{-\frac{t^2}{2}\right\}, \tag{6.53}$$

with $\omega = 5.5$. And for DWT, the Haar wavelet is used:

$$\psi_{\mathrm{Haar}}(t) = \begin{cases} 1 & 0 \le t < \frac{1}{2} \\ -1 & \frac{1}{2} \le t < 1 \\ 0 & \text{otherwise} \end{cases} \tag{6.54}$$

Scalogram

Scalogram or a wavelet periodogram is a two-dimensional, time-frequency (l, s) representation of the energy-density map:

$$P_{\mathrm{waw}}(s,l) = |W(s,l)|^2, \tag{6.55}$$

therefore it shows the temporal localization of a frequency present in the signal $x(t)$.

Cone of Influence

The zone of errors is called the cone of influence (COI), and the border can be obtained as the distance from the highest peak of the auto-correlation of the wavelet's power to the point where it decays to e^{-1} of the peak's height. A conservative choice is to extend the COI to $3s$.

Irregularly Sampled Time Series

For unevenly sampled time series a Welch overlapping segment averaging (WOSA) can be implemented. WOSA consists of segmenting the time series into overlapping segments, taking the periodogram on each segment, and taking the average of all the periodograms. The COI is defined as those $\{l,s\}$ that satisfy:

$$|l - t_{\mathrm{m}}| \leq 3\omega s, \tag{6.56}$$

where $m = min$ and $m = max$. Maximum scale that can be probed is then

$$s_{\max} = \frac{t_{\max}\, t_{\min}}{6\omega}. \tag{6.57}$$

Bibliography

R. Arcodia, A. Merloni, K. Nandra, J. Buchner, M. Salvato, D. Pasham, R. Remillard, J. Comparat, G. Lamer, G. Ponti, A. Malyali, J. Wolf, Z. Arzoumanian, D. Bogensberger, D. A. H. Buckley, K. Gendreau, M. Gromadzki, E. Kara, M. Krumpe, C. Markwardt, M. E. Ramos-Ceja, A. Rau, M. Schramm, and A. Schwope. X-ray quasi-periodic eruptions from two previously quiescent galaxies. , 592(7856):704–707, April 2021. doi: 10.1038/s41586-021-03394-6. URL https://ui.adsabs.harvard.edu/abs/2021Natur.592..704A.

R. Arcodia, Z. Liu, A. Merloni, A. Malyali, A. Rau, J. Chakraborty, A. Goodwin, D. Buckley, J. Brink, M. Gromadzki, Z. Arzoumanian, J. Buchner, E. Kara, K. Nandra, G. Ponti, M. Salvato, G. Anderson, P. Baldini, I. Grotova, M. Krumpe, C. Maitra, J. C. A. Miller-Jones, and M. E. Ramos-Ceja. The more the merrier: Srg/erosita discovers two further galaxies showing x-ray quasi-periodic eruptions, 2024. URL https://doi.org/10.48550/arXiv.2401.17275.

Roger Barlow. Asymmetric statistical errors, 2004. URL https://doi.org/10.48550/arXiv.physics/0406120.

Volker Beckmann and Chris R. Shrader. *Active Galactic Nuclei*. 2012. URL https://ui.adsabs.harvard.edu/abs/2012agn..book.....B.

Joheen Chakraborty, Erin Kara, Megan Masterson, Margherita Giustini, Giovanni Miniutti, and Richard Saxton. Possible x-ray quasi-periodic eruptions in a tidal disruption event candidate. *The Astrophysical Journal Letters*, 921(2):L40, November 2021. ISSN 2041-8213. doi: 10.3847/2041-8213/ac313b. URL http://dx.doi.org/10.3847/2041-8213/ac313b.

Franchini, Alessia, Bonetti, Matteo, Lupi, Alessandro, Miniutti, Giovanni, Bortolas, Elisa, Giustini, Margherita, Dotti, Massimo, Sesana, Alberto, Arcodia, Riccardo, and Ryu, Taeho. Quasi-periodic eruptions from impacts between the secondary and a rigidly precessing accretion disc in an extreme mass-ratio inspiral system. *AA*, 675:A100, 2023. doi: 10.1051/0004-6361/202346565. URL https://doi.org/10.1051/0004-6361/202346565.

Juhan Frank, Andrew King, and Derek J. Raine. *Accretion Power in Astrophysics: Third Edition*. 2002.

Suvi Gezari. The tidal disruption of stars by supermassive black holes. *Physics Today*, 67 (5):37–42, 05 2014. ISSN 0031-9228. doi: 10.1063/PT.3.2382. URL https://doi.org/10.1063/PT.3.2382.

Margherita Giustini, Giovanni Miniutti, and Richard D. Saxton. X-ray quasi-periodic eruptions from the galactic nucleus of RX J1301.9+2747. *A&A*, 636:L2, April 2020. doi: 10.1051/0004-6361/202037610. URL https://ui.adsabs.harvard.edu/abs/2020A&A...636L...2G.

Muryel Guolo, Dheeraj R. Pasham, Michal Zajaček, Eric R. Coughlin, Suvi Gezari, Petra Suková, Thomas Wevers, Vojtěch Witzany, Francesco Tombesi, Sjoert van Velzen, Kate D. Alexander, Yuhan Yao, Riccardo Arcodia, Vladimír Karas, James C. A. Miller-Jones, Ronald Remillard, Keith Gendreau, and Elizabeth C. Ferrara. X-ray eruptions every 22 days from the nucleus of a nearby galaxy. *Nature Astronomy*, January 2024. ISSN 2397-3366. doi: 10.1038/s41550-023-02178-4. URL http://dx.doi.org/10.1038/s41550-023-02178-4.

Kayhan Gültekin, Douglas O. Richstone, Karl Gebhardt, Tod R. Lauer, Scott Tremaine, M. C. Aller, Ralf Bender, Alan Dressler, S. M. Faber, Alexei V. Filippenko, Richard Green, Luis C. Ho, John Kormendy, John Magorrian, Jason Pinkney, and Christos Siopis. Them- andm-lrelations in galactic bulges, and determinations of their intrinsic scatter. *The Astrophysical Journal*, 698(1):198–221, May 2009. ISSN 1538-4357. doi: 10.1088/0004-637x/698/1/198. URL http://dx.doi.org/10.1088/0004-637X/698/1/198.

Adam Ingram, Sara E. Motta, Suzanne Aigrain, and Aris Karastergiou. A self-lensing binary massive black hole interpretation of quasi-periodic eruptions. *MNRAS*, 503(2): 1703–1716, May 2021. doi: 10.1093/mnras/stab609. URL https://ui.adsabs.harvard.edu/abs/2021MNRAS.503.1703I.

Vladimir Karas, Jiri Svoboda, and Michal Zajacek. Selected chapters on active galactic nuclei as relativistic systems, 2021.

Karamveer Kaur, Nicholas C Stone, and Shmuel Gilbaum. Magnetically dominated discs in tidal disruption events and quasi-periodic eruptions. *Monthly Notices of the Royal Astronomical Society*, 524(1):1269–1290, June 2022. ISSN 1365-2966. doi: 10.1093/mnras/stad1894. URL http://dx.doi.org/10.1093/mnras/stad1894.

Shubham Kejriwal, Vojtech Witzany, Michal Zajacek, Dheeraj R. Pasham, and Alvin J. K. Chua. Repeating nuclear transients as candidate electromagnetic counterparts of lisa extreme mass ratio inspirals, 2024. URL https://doi.org/10.48550/arXiv.2404.00941.

Andrew King. Quasi-periodic eruptions from galaxy nuclei. , 515(3):4344–4349, September 2022. doi: 10.1093/mnras/stac1641. URL https://ui.adsabs.harvard.edu/abs/2022MNRAS.515.4344K.

Julian H. Krolik and Itai Linial. Quasiperiodic Erupters: A Stellar Mass-transfer Model for the Radiation. , 941(1):24, December 2022. doi: 10.3847/1538-4357/ac9eb6. URL https://ui.adsabs.harvard.edu/abs/2022ApJ...941...24K.

Itai Linial and Brian D. Metzger. Emri + tde = qpe: Periodic x-ray flares from star-disk collisions in galactic nuclei, 2023. URL https://doi.org/10.48550/arXiv.2303.16231.

Itai Linial and Re'em Sari. Unstable Mass Transfer from a Main-sequence Star to a Supermassive Black Hole and Quasiperiodic Eruptions. , 945(2):86, March 2023. doi: 10.3847/1538-4357/acbd3d. URL https://ui.adsabs.harvard.edu/abs/2023ApJ...945...86L.

Brian D. Metzger, Nicholas C. Stone, and Shmuel Gilbaum. Interacting stellar emris as sources of quasi-periodic eruptions in galactic nuclei. *The Astrophysical Journal*, 926 (1):101, feb 2022. doi: 10.3847/1538-4357/ac3ee1. URL https://dx.doi.org/10.3847/1538-4357/ac3ee1.

G. Miniutti, R. D. Saxton, M. Giustini, K. D. Alexander, R. P. Fender, I. Heywood, I. Monageng, M. Coriat, A. K. Tzioumis, A. M. Read, C. Knigge, P. Gandhi, M. L. Pretorius, and B. Agís-González. Nine-hour X-ray quasi-periodic eruptions from a low-mass black hole galactic nucleus. *NAT*, 573(7774):381–384, September 2019. doi: 10.1038/s41586-019-1556-x. URL https://ui.adsabs.harvard.edu/abs/2019Natur.573..381M.

G. Miniutti, M. Giustini, R. Arcodia, R. D. Saxton, J. Chakraborty, A. M. Read, and E. Kara. Alive and kicking: A new qpe phase in gsn 069 revealing a quiescent luminosity threshold for qpes. *Astronomy amp; Astrophysics*, 674:L1, May 2023. ISSN 1432-0746. doi: 10.1051/0004-6361/202346653. URL http://dx.doi.org/10.1051/0004-6361/202346653.

Ramesh Narayan. Hydrodynamic Drag on a Compact Star Orbiting a Supermassive Black Hole. , 536(2):663–667, June 2000. doi: 10.1086/308956. URL https://ui.adsabs.harvard.edu/abs/2000ApJ...536..663N.

Priyamvada Natarajan. The first monster black holes. *Scientific American*, 318:24–29, 02 2018. doi: 10.1038/scientificamerican0218-24. URL http://dx.doi.org/10.1038/scientificamerican0218-24.

Nadine Neumayer, Anil Seth, and Torsten Böker. Nuclear star clusters. *The Astronomy and Astrophysics Review*, 28(1), July 2020. ISSN 1432-0754. doi: 10.1007/s00159-020-00125-0. URL http://dx.doi.org/10.1007/s00159-020-00125-0.

Xin Pan, Shuang-Liang Li, Xinwu Cao, Giovanni Miniutti, and Minfeng Gu. A disk instability model for the quasi-periodic eruptions of gsn 069. *The Astrophysical Journal Letters*, 928(2):L18, April 2022. ISSN 2041-8213. doi: 10.3847/2041-8213/ac5faf. URL http://dx.doi.org/10.3847/2041-8213/ac5faf.

D. R. Pasham, E. R. Coughlin, M. Zajaček, Itai Linial, Petra Suková, C. J. Nixon, Agnieszka Janiuk, M. Sniegowska, Vojtěch Witzany, V. Karas, M. Krumpe, D. Altamirano, T. Wevers, and Riccardo Arcodia. Alive but barely kicking: News from 3+ yr of swift and xmm-newton x-ray monitoring of quasiperiodic eruptions from ero-qpe1. *The Astrophysical Journal Letters*, 963(2):L47, March 2024. ISSN 2041-8213. doi: 10.3847/2041-8213/ad2a5c. URL http://dx.doi.org/10.3847/2041-8213/ad2a5c.

P. C. Peters. Gravitational Radiation and the Motion of Two Point Masses. *Physical Review*, 136(4B):1224–1232, November 1964. doi: 10.1103/PhysRev.136.B1224. URL https://ui.adsabs.harvard.edu/abs/1964PhRv..136.1224P.

A. Raj and C. J. Nixon. Disk tearing: Implications for black hole accretion and agn variability. *The Astrophysical Journal*, 909(1):82, mar 2021. doi: 10.3847/1538-4357/abdc25. URL https://dx.doi.org/10.3847/1538-4357/abdc25.

C. Megan Urry and Paolo Padovani. Unified Schemes for Radio-Loud Active Galactic Nuclei. *PASP*, 107:803, September 1995. doi: 10.1086/133630. URL https://ui.adsabs.harvard.edu/abs/1995PASP..107..803U.